Redox Biology 47 (2021) 102151

Contents lists available at ScienceDirect

Redox Biology

journal homepage: www.elsevier.com/locate/redox

N^6-methyladenosine modification regulates ferroptosis through autophagy signaling pathway in hepatic stellate cells

Min Shen [a], Yujia Li [a], Yingqian Wang [a], Jiangjuan Shao [a], Feng Zhang [a,b], Guoping Yin [c], Anping Chen [d], Zili Zhang [a,b,*], Shizhong Zheng [a,b,**]

[a] Jiangsu Key Laboratory for Pharmacology and Safety Evaluation of Chinese Materia Medica, Nanjing University of Chinese Medicine, Nanjing, 210023, China
[b] Jiangsu Key Laboratory of Therapeutic Material of Chinese Medicine, Nanjing University of Chinese Medicine, Nanjing, 210023, China
[c] Department of Anesthesiology, Nanjing Hospital Affiliated to Nanjing University of Chinese Medicine, Nanjing, China
[d] Department of Pathology, School of Medicine, Saint Louis University, St Louis. MO, 63104, USA

ARTICLE INFO

Keywords:
Ferroptosis
Autophagy
Hepatic stellate cell
Liver fibrosis
m6A modification
YTHDF1

ABSTRACT

Ferroptosis is a recently identified non-apoptotic form of cell death characterized by iron-dependent lipid peroxidation. However, the underlying exact mechanisms remain poorly understood. Here, we report that the total levels of N^6-methyladenosine (m^6A) modification are evidently increased upon exposure to ferroptosis-inducing compounds due to the upregulation of methylase METTL4 and the downregulation of demethylase FTO. Interestingly, RNA-seq shows that m^6A modification appears to trigger autophagy activation by stabilizing BECN1 mRNA, which may be the potential mechanism for m^6A modification-enhanced HSC ferroptosis. Importantly, YTHDF1 is identified as a key m^6A reader protein for BECN1 mRNA stability, and knockdown of YTHDF1 could prevent BECN1 plasmid-induced HSC ferroptosis. Noteworthy, YTHDF1 promotes BECN1 mRNA stability and autophagy activation via recognizing the m^6A binding site within BECN1 coding regions. In mice, erastin treatment alleviates liver fibrosis by inducing HSC ferroptosis. HSC-specific inhibition of m^6A modification could impair erastin-induced HSC ferroptosis in murine liver fibrosis. Moreover, we retrospectively analyzed the effect of sorafenib on HSC ferroptosis and m^6A modification in advanced fibrotic patients with hepatocellular carcinoma (HCC) receiving sorafenib monotherapy. Attractively, the m^6A modification upregulation, autophagy activation, and ferroptosis induction occur in human HSCs. Overall, these findings reveal novel signaling pathways and molecular mechanisms of ferroptosis, and also identify m^6A modification-dependent ferroptosis as a potential target for the treatment of liver fibrosis.

1. Introduction

Liver fibrosis is a complex physiological and pathophysiological condition associated with the mechanisms of cicatrization [1]. The deposition of extracellular matrix is a central event in liver fibrosis, and the myofibroblasts matrix is mainly produced by activated HSCs [2]. Consequently, elimination of HSCs is a main therapeutic strategy in the development of anti-fibrotic therapy [3]. We previously reported that the pathological and pathophysiological condition of liver fibrosis could alleviated by triggering the activation of apoptosis [4], senescence [5], necroptosis [6], lipocyte phenotype [7], and prevention of the proliferation [8], contractile [9], glycolytic [10] and pericyte [11] in HSCs. Interestingly, ferroptosis is thought to be a new and effective approach for scavenging HSCs in our recent research. We found that RNA binding proteins ELAVL1 and ZFP36 could trigger HSC ferroptosis to alleviate liver fibrosis by regulating autophagy pathway [12,13]. Moreover, we also revealed that mitochondrial iron metabolism pathway may regulate HSC ferroptosis via BRD7/P53/SLC25A28 axis [14]. The aim of the present study was to evaluate the potential mechanisms of ferroptosis and its role in the inhibition of liver fibrosis.

Distinct from classic morphological features of apoptosis, necrosis, necroptosis, pyroptosis, and senescence, ferroptosis is a recently identified form of programmed cell death [15]. Iron-depended lipid peroxidation, glutathione peroxidase 4 (GPX4) deletion and condensed mitochondrial membrane densities are the main characteristics of ferroptosis [16]. Attractively, system X_c^- inhibition (such as sulfasalazine,

* Corresponding author. Nanjing University of Chinese Medicine, 138 Xianlin Avenue, Nanjing, Jiangsu, 210023, China.
** Corresponding author. Nanjing University of Chinese Medicine, 138 Xianlin Avenue, Nanjing, Jiangsu, 210023, China.
E-mail addresses: zilizhang@njucm.edu.cn (Z. Zhang), nytws@163.com (S. Zheng).

https://doi.org/10.1016/j.redox.2021.102151
Received 10 September 2021; Accepted 24 September 2021
Available online 26 September 2021

sorafenib, erastin), GPX4 inhibition (such as FIN56, altretamine, RSL3, FINO2), and physiological conditions (such as cystine deprivation, amino acid starvation, high extracellular glutamate) are reported to induce ferroptosis [17]. Importantly, the crosstalk between ferroptosis and autophagy has received increasing concern, and autophagy is a targeted pathway that regulates the cellular sensitivity to ferroptosis [18]. Although transcriptional regulation of autophagy signaling pathways in ferroptosis has been elucidated well, the function of post-transcriptional regulation in ferroptosis remains poorly known.

The m^6A RNA modification serves as the most abundant post-transcriptional mechanism in eukaryotic messenger RNAs (mRNAs), which is a reversible process controlled by methyltransferase, demethylases and m^6A binding proteins. The methyltransferase complex catalyzes m^6A mRNA methylation that contains WT1 associated protein (WTAP), methyltransferase like 3 (METTL3), METTL4, and METTL14. In contrast, alkB homolog 5 (ALKBH5) and obesity-associated protein (FTO) function as demethylases to remove m^6A modifications from RNA and thus keep m^6A modification in a dynamic balance. Additionally, m^6A binding proteins including heterogeneous nuclear ribonucleoprotein A2/B1 (HNRNPA2B1), insulin-like growth factor 2 mRNA-binding proteins (IGF2BPs), YTH-domain- containing protein 1/2 (YTHDC1/2), and YTH domain family 1/2/3 (YTHDF1/2/3) bind to the m^6A motif to affect RNA stability or function [19]. Interestingly, exploring the post-transcriptional regulation of m^6A-mediated HSC ferroptosis may provide therapeutic targets and effective diagnostic signs for liver fibrosis.

In the present study, we investigated a novel signaling pathways and molecular mechanisms of ferroptosis in liver fibrosis. Our study revealed that m^6A reader YTHDF1 promoted the stability of BECN1 mRNA via recognizing the m^6A binding site, thus triggering autophagy activation, and eventually leading to HSC ferroptosis. We indicated that m^6A modification may be novel and critical post-transcriptional regulators of ferroptosis in liver fibrosis.

2. Materials and methods

2.1. Human liver specimens

From September 2015 and December 2020, we obtained liver resection tissues of ten patients with liver cirrhosis complicated with HCC treated with sorafenib monotherapy and liver biopsy specimens of ten patients with liver cirrhosis without any treatment were obtained in the Affiliated Hospital of Nanjing University of Chinese Medicine. The initial dose of sorafenib was 400 mg, taken orally twice daily after dinner and breakfast [21]. Subsequently, sorafinib was temporarily interrupted or reduced based on the toxicity and tolerance. Obtained written informed consent from patients. According to the electronic medical records, the data on the characteristics of patients were collected retrospectively. The diagnostic criteria for HCC and liver cirrhosis according to the American Association for the study of liver disease (AASLD) [20]. This research protocol complied with the ethical guidelines of the 1975 Declaration of Helsinki Principles and was approved by the ethics committee of Nanjing University of Chinese Medicine.

2.2. Isolation and characterization of primary human HSC

Laser capture microdissection was used to isolate primary HSCs from human liver tissue according to our reports previously [22]. Briefly, human liver tissue was stained with desmin (ab15200, Abcam) by immunofluorescence. Then, CapSure® LCM Cap (LCM0211, Thermo Fisher Scientific) was placed on the section. The cap was passed through by laser pulses, forming a thin protuberance of the thermoplastic film that connects the gap between the tissue and the cap and attaching it to the positive cells stained by the desmin. Target cells attached to the cap can be removed by lifting the cap. α-SMA (ab5694, Abcam) and platelet derived growth factor receptor beta (PDGFRB, ab32570, Abcam) were detected to confirm the characterization and purification of the obtained human HSCs.

2.3. Animal experiments

ICR mice (8-week-old, 18–22 g) were obtained from Yangzhou University (Yangzhou, China). There were 8 mice in each group and they were randomly divided into 6 groups. Mice were treated with Vehicle, CCl_4, VA-Lip-control-vector + CCl_4+Erastin, VA-Lip-Mettl4-shRNA + CCl_4+Erastin, VA-Lip-Fto-plasmid + CCl_4+Erastin, VA-Lip- Ythdf1-shRNA + CCl_4+Erastin, respectively. A mixture of olive oil and carbon tetrachloride (CCl_4) (9:1 (v/v)) was used to trigger liver fibrosis in mouse model by intraperitoneal injection (0.1 ml/20 g body weight), according to our previous reports [23]. Erastin was dissolved according to the instructions and given once every other day for 2 weeks by intraperitoneal injection (30 mg/kg) after the CCl_4 treatment. Within 2 weeks after CCl_4 treatment, VA-Lip-Mettl4-shRNA, VA-Lip-Fto-Plasmid and VA-Lip-Ythdf1-shRNA (0.75 mg/kg) were injected intravenously 3 times a week. The liver samples and blood of each group were collected at the end of the experiment. Fixation of a small portion of the liver with 4% Paraformaldehyde Fix Solution (PFS, P6148, Sigma-Aldrich) for histopathological studies. All in vivo experimental procedures were performed according to the institutional and local animal care and use committee of Nanjing University of Chinese Medicine (Nanjing, China).

2.4. Isolation and characterization of primary HSC

Primary mouse HSCs were isolated according to our previous reports [12,13]. In brief, DMEM-free solution containing pronase (2 mg/ml, PRON-RO, 10165921001, Roche) and collagenase IV (1 mg/ml, V900893, Vetec) were used to perfuse the liver in situ and following HBSS including EDTA (0.5 mM, E6758, Sigma-Aldrich). Upon completing the perfusion, the digested hepatocytes from the liver were dispersed in DMEM-free. Then, the filamentous gelatinous material was inhibited by using DNase enzyme (D4263, Sigma-Aldrich). The undigested debris was then removed by filter and centrifuged in 4 °C for 5 min at 50×*g*. 25% Histodenz (D2158, Sigma-Aldrich) gradient centrifugation, and the supernatant was collected to separate primary HSCs. Cells were inoculated on a culture dishes (CLS430599, Sigma-Aldrich) with a diameter of 60 mm. By detecting PDGFRB and α-SMA to identify and purity of the obtained HSCs.

2.5. Histological analyses

Liver tissue samples were paraffin embedded and 4 μm tissue sections stained with standard methods and subjected to histopathological analysis according to our reports previously [12]. Briefly, the samples were fixed in 4% PFS and then were transferred to different concentration of ethanol for dehydration. Hepatic morphology and liver fibrosis were examined by H&E, Masson, and Sirius red staining.

2.6. Reagents and antibodies

Ferrostatin-1 (S7243), necrostatin-1 (S8037), Z-VAD-FMK (S7023), liproxstatin-1 (S7699), sorafenib (S7397), erastin (S7242), RSL3 (S8155), MG-132 (S2619) were bought from Selleck Chemicals. CHX (C7698) and Act-D (129935) were purchased from Sigma-Aldrich. Anti-N^6-methyladenosine antibody (ab208577), anti-METTL3 antibody (ab195352), anti-METTL4 (ab107540), anti-METTL14 antibody (ab220030), anti-FTO antibody (ab92821), anti-ALKBH5 antibody (ab195377), anti-YTHDF1 antibody (ab220162), anti-YTHDF2 antibody (ab220163), anti-YTHDF3 antibody (ab220161), anti-YTHDC2 antibody (ab220160), anti-HNRNPA2B1 antibody (ab31645), anti-ATG3 antibody (ab108282), anti-ATG4A antibody (ab223374), anti-ATG5 antibody (ab108327), anti-BECN1 antibody (ab207612), anti-ATG7

antibody (ab133528), anti-ATG9A antibody (ab108338), anti-ATG12 antibody (ab155589), anti-ATG16L1 antibody (ab187671), anti-LC3-I/II antibody (ab128025), anti-P62 antibody (ab109012), anti-NCOA4 antibody (ab86707), anti-FTH1 antibody (ab65080), and anti-beta actin (ab6276) antibody were purchased from Abcam Technology. Anti-WTAP antibody (sc-374280) was bought from Santa Cruz Biotechnology. Anti-Mouse IgG (G-21040) and anti-Rabbit IgG (G-21234) were bought from Thermo Fisher Scientific.

2.7. Plasmid construction

The pcDNA3.1-FTO plasmid, pcDNA3.1-BECN1 plasmid, METTL4 shRNA (sc-75777-SH, sc-149388-SH), YTHDF1 shRNA (sc-76945-SH, sc-155423-SH) and control vector were obtained from KeyGEN BioTECH (KG20200903-10) and Santa Cruz Biotechnology, respectively. CMV-TurboRFP-EGFP-LC3-PGK-Puro plasmid (GM-1314L204H) and pGM-CMV-GFP-hLC3 (GM-1314P101H) were obtained from Genomeditech (Shanghai, China). According to our previous reports, VA-Lip-Mettl4 -shRNA, VA-Lip-Fto-plasmid, VA-Lip-Ythdf1-shRNA, and VA-Lip-Control-vector were prepared [12]. Briefly, VA solution was formed by 50 μl DMSO add 5 mg VA (95144, Sigma). 0.14 μmol lipotrust solution (LEO-01, Hokkaido System Science) and 280 nmol VA solution were mixed in tube (AM12450, Thermo Fisher Scientific) at 25 °C. Under the condition of stirring, 12.24 nmol Mettl4-shRNA, Fto-plasmid, Ythdf1-shRNA, and Control-vector were added into VA-Lip solution. Material trapped in the filter (596–3320, Thermo Fisher Scientific) and the fractions were collected to achieve the indicated dose for in vivo use.

2.8. Construction of BECN1 mutant plasmid

Mutations of BECN1 were constructed by PCR-based methods according to previous reports [24]. The 5′-UTR, 3′UTR, and CDS of BECN1 mRNA was synthesized and subcloned into the vector pCDNA3.1. Moreover, Adenine (A) 437 and Adenine (A) 1276 were mutated to Guanine (G). Briefly, the mutant of BECN1 was conducted by the following primer pairs: (A437G mutant) BECN1, forward 5′-CAGATACTCTTT TAGGCCAGCTGGACACTCA-3′ and reverse 5′-TGAGTGTCCAGCTGGCCT AAAAGAGTATCTG-3′, (A1276G mutant) BECN1, 5′-TCTGAGGAGCAGTGGGC AAAAGCTCTCAAGT-3′ and reverse 5′-ACTTG AGAGCTTTTGCCCACTGCTC CTCAGA-3'. BECN1 WT and mutants were confirmed by DNA sequencing.

2.9. Construction of stable cell lines

According to a reported protocol, stable cell lines were constructed [25]. Briefly, the HSCs were seeded in 6-well plates (CLS3516, Sigma-Aldrich). When cells reached 70% confluence, serum-free DMEM medium was replaced. Then, the plasmid and Lipofectamine 3000 transfection reagent mixture (L3000015, Invitrogen) were added into each well to initiate transfection. After 8 h, the medium containing 5% FBS was replaced. After the beginning of the transfection approximately 48 h, the cells were digested and the cell suspensions were plated onto 25 ml culture flasks (156367, Thermo Fisher Scientific). 5 μg/ml puromycin (A1113803, Thermo Fisher Scientific) were added in the medium for 7 days to select a stable cell line, and the efficacy was measured by western blot.

2.10. Drug treatment and cell culture conditions

HSC-T6 and HSC-LX2 lines were purchased from BeNa Culture Collections (Beijing, China), the primary HSCs were isolated from mouse liver. These cell lines were cultured in a humidified atmosphere containing 5% CO_2 at 37 °C and maintained in 10% FBS (A4766801, Gibco), 1% penicillin/streptomycin (C125C5, NCM Biotech), and 90% Dulbecco's Modified Eagle Medium (DMEM, 11965092, Gibco). HSC ferrotosis was induced by treating with RSL3 (2.5 μm), erastin (10 μm) and sorafenib (10 μm) for 24 h. Meanwhile, equivalent amount of DMSO without drugs were added to the cells served as a control.

2.11. Cell viability assay

2×10^3 cells were plated in 96-well plates and treated with the compounds erastin, sorafenib and RSL3. After incubation for the indicated time, the cell viability was assessed by Cell Counting Kit-8 (CCK8, C0042, Beyotime Institute of Biotechnology). Briefly, CCK8 reagent was added to each well, and the well without cells was used as the control. The cells were incubated for another 4 h at 37 °C, and the absorbance was measured at 450 nm.

2.12. Lipid ROS detection

HSCs were exposed to the compounds for the indicated time, and then stained with C11-BODIPY (D3861, Thermo Fisher Scientific) for 30 min according to the manufacturer's instructions. The well with no C11-BODIPY was used as control, then cells were washed and measured by flow cytometer (Beckman, CytoFLEX).

2.13. Lipid peroxidation assay

Cells of different treatment groups were lysed by freeze-thaw first and MDA was detected by lipid Peroxidation Assay Kit (ab118970, Abcam) according to our previous reports [12]. Briefly, the cell lysate supernatants were collected and 600 μl thiobarbituric acid (TBA) solution was added. The samples were incubated at 95 °C for 60 min. Each reaction mixture were transferred 200 μl into a 96-well plate, and the levels of MDA was detected by EnSpire Multimode Plate Reader (PerkinElmer, Waltham, MA, USA).

2.14. Iron assay

According to the manufacturer's instruction [26], Iron Assay Kit (ab83366, Abcam) was used to measure cellular iron concentration. In brief, 5×10^6 cells were seeded on to the plate and then pretreated with drugs for 24 h. Before centrifuging (13,000×*g*, 10 min) at 4 °C, cells were homogenized by 5 × volumes of iron assay buffer. Next, iron reducer and supernatant mixture were incubated at room temperature for 30 min. Then, each sample was added iron probe and incubated without light on the horizontal shaker for 60 min. The absorbance was detected at 593 nm by EnSpire Multimode Plate Reader (PerkinElmer, Waltham, MA, USA).

2.15. Glutathione assay

1×10^8 cells were seeded onto the plate and the relative GSH concentration were assayed according to our previous reports [12]. In brief, cells were washed with cold PBS and assayed according to the instructions using Glutathione Assay Kit (CS0260, Sigma-Aldrich). Then, 3 vol of the 5% SSA Solution were added and the samples were collected at 10000×*g* for 10 min. The supernatant was used to determine the amount of GSH. 150 μL GSH working mixture was added into each sample and incubated at room temperature for 5 min and then were added 50 μl of the diluted NADPH Solution. The yellow product (5-thio-2-nitrobenzoic acid) was measured at 412 nm by EnSpire Multimode Plate Reader (PerkinElmer, USA).

2.16. Quantification of RNA m^6A

The total RNA was isolated by TRIzol reagent (15596018, Invitrogen) according to the instructions of the manufacturer. The total m^6A RNA levels were detected by EpiQuik m^6A RNA Methylation Quantitative kit (Epigentek, Farmingdale, NY, USA). Firstly, 200 ng purified PolyA + mRNA was coated on assay wells. Then, RNA high binding

Table 1
Primer Sequences used for qRT-PCR.

Genes	Forward primer	Reverse primer
Human		
METTL3	5′-CAAGCTGCACTTCAGACGAA-3′	5′-GCTTGGCGTGTGGTCTTT-3′
METTL14	5′-AGAAACTTGCAGGGCTTCCT-3′	5′-TCTTCTTCATATGGCAAATTTTCTT-3′
METTL4	5′-TATCCCTCTTGGTCTGTGGAG-3′	5′-ACCTTCGTAGGGCTTTTTGTG-3′
WTAP	5′-GGCGAAGTGTCGAATGCT-3′	5′-CCAACTGCTGGCGTGTCT-3′
ALKBH5	5′-CGGCGAAGGCTACACTTACG-3′	5′-CCACCAGCTTTTGGATCACCA-3′
FTO	5′-ACTTGGCTCCCTTATCTGACC-3′	5′-TGTGCAGTGTGAGAAAGGCTT-3′
YTHDF1	5′-CAAGCACACAACCTCCATCTTCG-3′	5′-GTAAGAAACTGGTTCGCCCTCAT-3′
YTHDC1	5′-AGATGGGTCTGTCAGATCTGGT-3′	5′-TCTGAACCTGCATATGACTCTGAT-3′
ATG3	5′-CAGGCATGCTGAGGTGATGA-3′	5′-CGTTAACAGCCATTTTGCCACT-3′
ATG4A	5′-AAACCCCTGCTGCTCATTGT-3′	5′-ATGCCCCTAAAGACTGTGGC-3′
ATG5	5′-AAGACCTTCTGCACTGTCCATC-3′	5′-TGCAATCCCATCCAGAGTTGC-3′
ATG7	5′-TTGAGCGGCGGATCCAATTC-3′	5′-ATCTGGTGTCCATCAGCTTCAG-3′
BECN1	5′-AGGTACCGACTTGTTCCCTA-3′	5′-TCCATCCTGTACGGAAGACA-3′
ATG9A	5′-AGGGCTGGAGAGGAGCACATAC-3′	5′-GGCGACGTGCACCAACAG-3′
ATG12	5′-TGGAGGGGAAGGACTTACGG-3′	5′-TGGATGGTTCGTGTTCGCTC-3′
ATG14	5′-CTGTACGTGGCTGTGGAGC-3′	5′-TCTTGCTTGCTCTTAAGTCGGC-3′
ATG16	5′-CATCTCGGAGCAACTGAGGC-3′	5′-CCAGTTGAGCTAACTCCCCAC-3′
GAPDH	5′-AAATCCCATCACCATCTTCCAG-3′	5′-AGGGGCCATCCACAGTCTTCT-3′
Rat		
Mettl3	5′-CTTTAGCATCTGGTCTGGGCT-3′	5′-CCTTCTTGCTCTGCTGTTCCT-3′
Mettl14	5′-CTGGACCCACATTTGCGAGC-3′	5′-GGAAGCCCTGCAAGTTTCTCT-3′
Mettl4	5′-CTCGCCGAAGTTCTGAAAGACTA-3′	5′-AAACGAGCTGGGGTAAAGGC-3′
Wtap	5′-TAAGCTTGCAGAGCCCCCAC-3′	5′-CATCTTGTACCCCGAGACGC-3′
Alkbh5	5′-TGAGATCCCGGAATGGGTGC-3′	5′-CCGAAGCAAAGTGCCGAGTC-3′
Fto	5′-TCATGGGACATCGAGACGCC-3′	5′-TCCAAGGTGCCTGTTGAGCA-3′
Ythdf1	5′-GGACAGTCCAATCCGAGTAACA-3′	5′-GTGAGATACGGGATGGGAGG-3′
Ythdc1	5′-TGCCAAAGCAAAGGGTGTATG-3′	5′-TGATGACAATCTGGCAAAACCTT-3′
Atg3	5′-GAGGCTACCCTAGACACCAGA-3′	5′-TGTTAAAGGCTGCCGTTGCT-3′
Atg4a	5′-TTCGCCTGGGCATAAACCAA-3′	5′-GAAGGTCTGGGTTGTGTGAGG-3′
Atg5	5′-TGATCCCGGTAGACCCAACC-3′	5′-CCACACGTCTCGAAGCACAT-3′
Atg7	5′-GCGGATGTATGGACCCCAAA-3′	5′-GGAGATCTTGGCGTTGTCCA-3′
Becn1	5′-TTGGCCAATAAGATGGGTCTGAA-3′	5′-TGTCAGGGACTCCAGATACGAGTG-3′
Atg9a	5′-GCGAGGCTGGTAACTGGAATC-3′	5′-TACGCATCGCGAGCTCACTT-3′
Atg12	5′-CTGTCCAAGCACTCATCGACT-3′	5′-ATCCCCATGCCTGTGATTTGC-3′
Atg14	5′-GCCATGGAAGGAAAACGGCT-3′	5′-AAACACGCCAACCGATCGTA-3′
Atg16	5′-AATATCTTTGGGAGACGCTCTGTC-3′	5′-CTGCATTGACCTCTCCGTCAT-3′
Actb	5′-TTCTACAATGAGCTGCGTGTG-3′	5′-GGGGTGTTGAAGGTCTCAAA-3′

solution was used to bind total RNA to the strip wells. The capture and detection antibodies were used to detect the m^{6}A levels. Detection of the enhanced signal by reading the absorbance in the microplate spectrophotometer, followed by colorimetric quantification.

2.17. Dolt blot

According to previous reports, dot blots were performed with m^{6}A immunoblotting [27]. Briefly, RNA is mixed with the same amount of 20 × SSC buffer (Sigma-Aldrich) and incubated at 95 °C for 5 min. Then, 100 ng, 200 ng or 400 ng poly (A) + RNAs were added on Hybond N+ membranes (GE Healthcare). After UV crosslinking for 30 min. After blocking in 5% milk the membranes were then incubated with m^{6}A antibody overnight at 4 °C. Then, they were incubated with secondary antibody and applied with ECL for development. The same amount of RNA was also added on the membrane and stained with 0.02% methylene blue for 2 h.

2.18. Western blot

For western blot analysis, HSCs were lysed in RIPA buffer containing 50 mM Tris pH 7.4, 1% NP-40, 0.1% SDS, 0.5% sodium deoxycholate, 150 mM NaCl and protease inhibitors (P8340, Sigma-Aldrich). Protein concentration from supernatant was quantified by the BCA Protein Assay Kit (23250, Thermo Fisher Scientific). Proteins were separated and transferred to PVDF membranes, and blocked for 30 min in 5% milk and blotted with related antibodies in 4 °C overnight. The membranes were incubated with secondary antibody for 1 h. Protein bands were exposed using the chemiluminescence system (Bio-Rad, Hercules, CA).

2.19. RNA extraction and real-time PCR

TRIzol reagent was used to isolated the total RNA from liver tissues or cells according to the instructions (15596018, Invitrogen). The purity and concentration of RNA were measured using Nanodrop. Then, Hifair® II 1st Strand CDNA Synthesis Super Mix (11123ES60, YEASEN) was used to synthesize the template complementary DNA from total RNA. The QuantiTect SYBR Green PCR Kit Hieff qPCR SYBR Green Master Mix (11202ES08, YEASEN) was used to analyze the cDNA by qRT-PCR on ABI 7500 system (Applied Biosystems). Fold change was calculated using 2^{-ddCt} and GAPDH levels were taken for normalization. The primers were showed in Table 1.

2.20. Trypan blue staining

According to our previous reports [12], trypan blue staining was assayed. In brief, HSC-LX2 cells were cultured in 24-well plates and petreated with vehicle, erastin, sorafenib and RSL3 for 24 h. After treated indicated time, the cells were stained with trypan blue solution (KGY015, KeyGEN BioTECH). ImageJ software was used to quantify trypan blue-positive ratio in 10 random regions.

2.21. Transmission electron microscopy

According to our previous reports [12], morphological characteristics of HSC ferroptosis was performed by transmission electron microscopy assay. In brief, HSC-LX2 cells (20,000 cells/well) were cultured and inoculated onto 4-well Chambered Coverglass (155382, Thermo Fisher Scientific). Olympus EM208S transmission electron microscope

was used to acquire the images.

2.22. RNA sequencing

Total RNA was isolated from HSC-LX2 cells by TRIzol reagent (15596018, Invitrogen). For each sample, TruSeq Stranded Total RNA with 1 μg RNA was used for library preparation with Ribo-Zero Gold kit (MRZG12324, Illumina). TopHat v1.4.1 was used to align the reads of each sample with the human reference genome (GRCh38.p10). EdgeR version 3.08 was performed for differential gene expression. The Benjamini-Hochburg method was used to calculate the adjusted P values. We used fold change <0.65 for downregulationn and fold change >1.4 for upregulatio as cutoffs.

2.23. MeRIP qPCR

According to a reported protocol, m^6A immunoprecipitation (MeRIP) qPCR was performed [27]. In brief, normal rabbit IgG and 5 μg m^6A antibody were conjugated to 50 μl Protein A/G Plus Agarose overnight at 4 °C, respectively. The antibody was incubated with 100 μg fragmented total RNA in immunoprecipitation buffer (0.5% NP40, 50 mM Tris-HCl and 750 mM NaCl) added 40U RNase inhibitor (2313Q, Takara) at 4 °C overnight. After incubation with 300 μl elution buffer (0.05% SDS, 1 mM EDTA and 5 mM Tris-HCl) with 8.4 μg proteinase K (9034, Takara) at 50 °C for 1.5 h, RNAs were eluted from the beads. Following TRIzol and ethanol precipitation, the enrichment was measured by real-time PCR after the input and m^6A-enriched RNAs were reversely transcribed.

2.24. Immunofluorescence

For immunofluorescence staining [12], HSC-LX2 were cultured in 24-well plates and treated with the compounds for the indicated time. Then, they were incubated with antibody against LC3 (ab48394, Abcam) overnight. Thereafter, FITC-labeled secondary antibodies (ab6717, Abcam Technology) were added. Nuclear counterstaining was assayed with DAPI (KGA215-50, KeyGEN BioTECH) and the images were taken with the fluorescence microscopy or confocal microscopy.

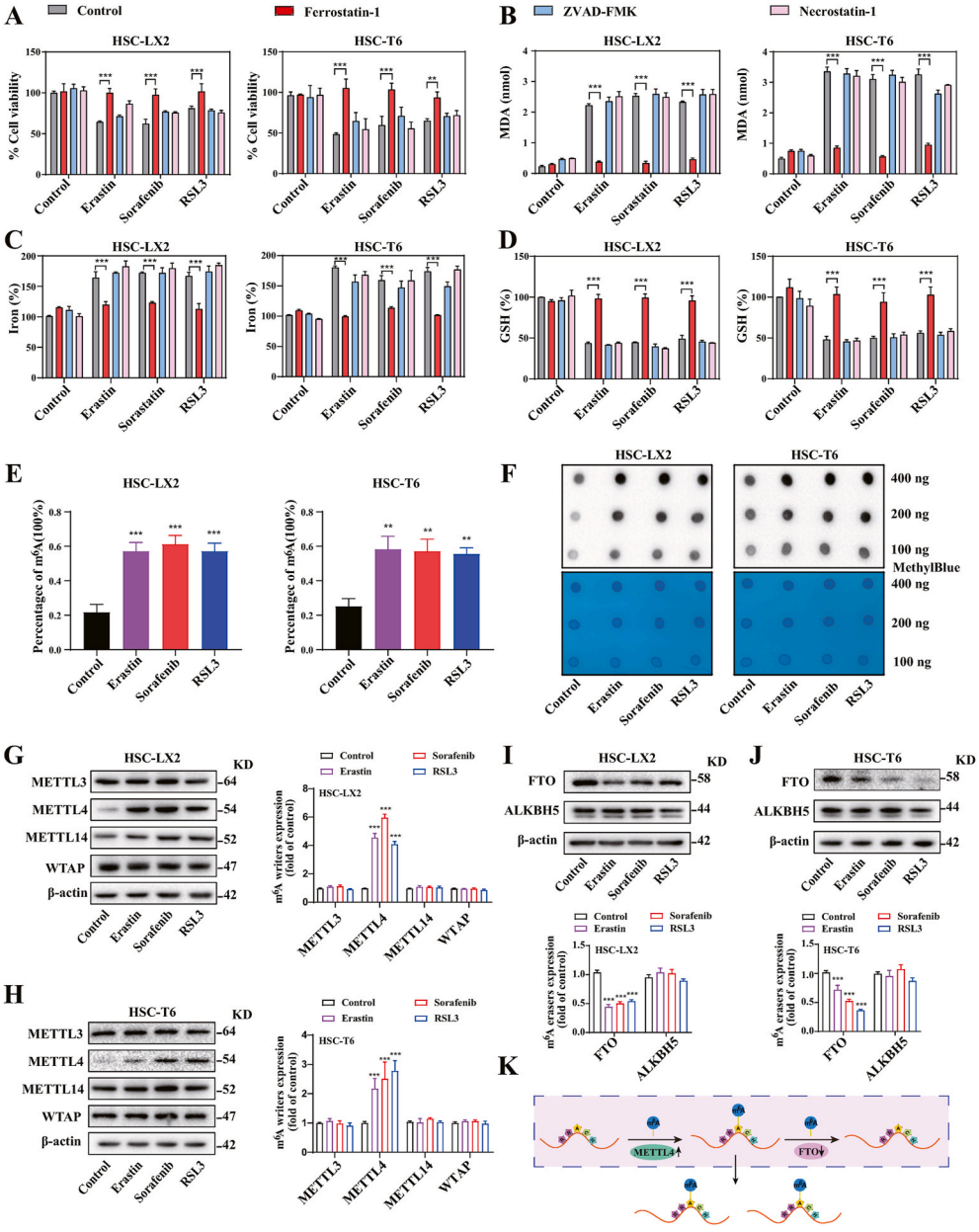

Fig. 1. m^6A modification is up-regulated during HSC ferroptosis. HSC-T6 and HSC-LX2 cells were treated with RSL3 (2.5 μM), sorafenib (10 μM), and erastin (10 μM), with or without the addition of Ferrostatin-1 (1 μM), Necrostatin-1 (10 μM), ZVAD-FMK (10 μM) for 24 h. (**A**) Cell Counting Kit-8 kit was used to determine the Cell viability (**, $p < 0.01$, ***, $p < 0.001$, $n = 3$ in every group). (**B-D**) MDA production, iron accumulation, and GSH levels were measured by commercial kits (***, $p < 0.001$, $n = 3$ in every group). (**E, F**) m^6A RNA Methylation Quantitative kit and dot blot were used to detect the m^6A modification (**, $p < 0.01$, ***, $p < 0.001$, $n = 3$ in every group). (**G, H**) Western blot showed the protein levels of m^6A writers. (***, $p < 0.001$, $n = 3$ in every group). (**I, J**) The protein levels of m^6A erasers were determined by western blot (***, $p < 0.001$, $n = 3$ in every group). (**K**) The mechanism of the increased m^6A modification in RNA was showed.

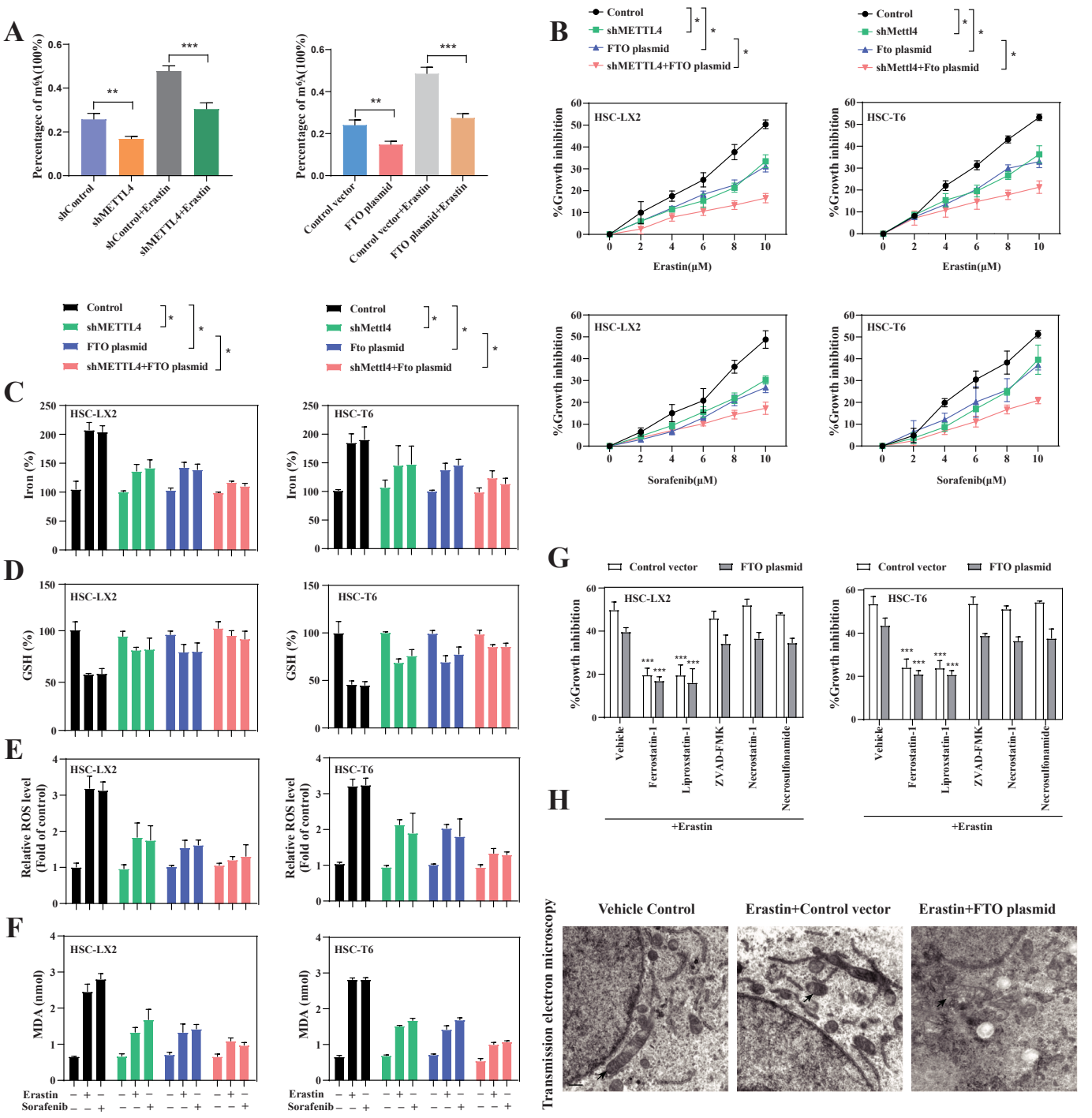

Fig. 2. Inhibition of m^{6}A modification confers resistance to HSC ferroptosis. METTL4 shRNA or FTO plasmid were stably transfected into HSC-LX2 cells followed by erastin (10 μM) treatment for 24 h. (**A**) The m^{6}A levels were detected by m^{6}A RNA Methylation Quantitative kit (**, $p < 0.01$, ***, $p < 0.001$, $n = 3$ in every group). (**B**) METTL4 shRNA or FTO plasmid were transfected into HSC-LX2 and HSC-T6 cells followed by sorafenib (10 μM) or erastin (10 μM) treatment for 24 h. Cell Counting Kit-8 kit was used to determine the Cell viability (*, $p < 0.05$, $n = 3$ in every group). (**C–F**) Iron accumulation, GSH depletion, lipid ROS level and MDA production were assayed (*, $p < 0.05$, $n = 3$ in every group). (**G**) FTO plasmid transfected into HSC-LX2 and HSC-T6 cells were treated with erastin (10 μM) with or without the indicated inhibitors (Liproxstatin-1, 100 nM; Ferrostatin-1, 1 μM; Necrostatin-1, 10 μM; ZVAD-FMK, 10 μM; Necrosulfonamide, 0.5 μM) for 24 h. Cell viability was assayed by Cell Counting Kit-8. (***, $p < 0.001$, $n = 3$ in every group). (**H**) Control vector or FTO plasmid were transfected into HSC-LX2 cells and treated with erastin (10 μM) for 24 h. Transmission electron microscopy was used to examin the typical changes of ferroptotic cells. Scale bars: 0.2 μm. Representative photographs were showed.

2.25. *Long-lived protein degradation analysis*

According to our previous reports [13], LC-MS/MS was used to determine the rate of long-lived protein degradation. In brief, the HSC-LX2 cells transfected with METTL4 shRNA or FTO plasmid, and labeled with L-[$^2H_4$] lysine, or L-[U–$^{13}C_6$, $^{15}N_4$] arginine and L-arginine and L-lysine, L-[U–$^{13}C_6$, $^{14}N_4$] arginine and L-[U–$^{13}C_6$, $^{15}N_2$] lysine (74-79-3, Cambridge Isotope Laboratories; 23128, Sigma-Aldrich). Then, the cell scraping buffer containing 1 mM sodium orthovanadate (S6508, Sigma-Aldrich), 0.25 M sucrose (BP818, Sigma-Aldrich), 5 mM

β-glycerophosphate (G5422, Sigma-Aldrich), 5 mM NaF (S7920, Sigma-Aldrich), and protease inhibitor mixture (04693132001, Roche) were added. Before samples were concentrated on spin tubes (CLS8160, Sigma-Aldrich), the mixed cells were centrifuged and lysed in 2% benzonase (E1014, Sigma-Aldrich), 2 M thiourea (PHR1758, Sigma-Aldrich), and 6 M urea (U5378, Sigma-Aldrich). The mixed proteins were separated by SDS-PAGE. Gel lanes were cut into 15 pieces, and the samples were digested in the gel. The peptide mixtures obtained were STAGE-tipped. LC-MS/MS was used to detect the identification and relative quantification of peptides.

2.26. Cycloheximide chase assay

To measure BECN1 protein stability, HSC-LX2 cells were treated with 100 μg/ml cycloheximide (C7698, Sigma-Aldrich) during indicated times after treatment with 10 μM erastin for 24 h. The stability of BECN1 was detected through western blot analysis as described previously [28].

2.27. RIP-RT-PCR

According to a reported protocol [28], RNA immunoprecipitation (RIP) was performed. In brief, cells were irradiated twice at 254 nm with 400 mJ/cm^2 by Stratalinker. After washing with cold PBS, cells were lysed in high salt lysis buffer (0.5 mM DTT, 0.2% NP-40, 300 mM NaCl, 20 mM Tris-HCl PH 7.6, 200U/ml RNase inhibitor, and protease inhibitor) for 30 min at 4 °C. After treatment with 1 U RNase T1(EN0541, Thermo Fisher Scientific) at 24 °C for 15 min, the supernatant was incubated with Protein A/G Plus Agarose (sc-2003, Santa Cruz Biotechnology), or anti-YTHDF1 antibody in 500 μl 1 × IP buffer supplemented with RNase inhibitors overnight at 4 °C. Then, 100 μL of elution buffer (20 mg/ml Proteinase K, 0.05% SDS, 1 mM EDTA pH 8.0, 5 mM Tris-HCL pH 7.5) was added for 2 h at 50 °C. RNAs associated with YTHDF1 were recovered by TRIzol and ethanol precipitation and detected by real-time PCR.

2.28. Biotinylated RNA pull-down assay

According to our previous reports [13], the proteins bound to the RNA and synthesis of biotinylated transcripts were detected. Briefly, template for PCR amplification of the 5'-UTR, CDS, and 3'-UTR of BECN1 mRNA were obtained from cDNA of HSC-LX2 cells. Cells were washed twice with cold PBS, harvested and lysed in cell lysis. Then, whole cell lysates (120 μg per sample) were incubated with biotinylated transcripts (9 μg) for 30 min at 30 °C. Paramagnetic streptavidin-conjugated Dynabeads (11206D, Dynal) was used to isolate the complexes and analyzed by western blot.

2.29. Luciferase reporter system construction

As described previously [12], 3′-UTR, 5′-UTR and CDS of human BECN1 were cloned into pGL3-Luc vector (E1751, Promega). Then, pGL3-Luc-BECN1-3′UTR, pGL3-Luc-BECN1-CDS and pGL3-Luc--BECN1-5′UTR plasmids were transfected into cells. To monitor transfection efficiencies, the luciferase reporter vectors were transfected in cells together with phRL-null (E2231, Promega).

2.30. Calculations and statistics

The matched controls was used for individual animal experiments and cell experiments, performed in duplicate or triplicate and repeated 3 times, and the data were pooled. Data were expressed as mean ± standard error of the mean (SEM). Statistical analysis was performed using either one-way or Student's t-test (two-group comparison) analyses of variance followed by Student-Newman-Keuls test (more than two groups). In all analysis, a probability of less than 0.05 was considered to indicate statistical significance. GraphPad Prism 8 (GraphPad software version 8.0) was used for all statistical analyses.

3. Results

3.1. m^{6}A modification is up-regulated during HSC ferroptosis

Our previous studies showed that preclinical and clinical drugs (e.g., sorafenib and erastin) can induce HSC ferroptosis [12]. Consistent with our previous findings [16,29], treatment with erastin, sorafenib, and RSL3 evidently inhibited cell viability in both rat (HSC-T6), human (HSC-LX2) HSC cells and primary HSCs, but ferroptosis inhibitor (ferrostatin-1) rather than necroptosis inhibitor (necrostatin-1) and apoptosis inhibitor (ZVAD-FMK) completely rescued the cell growth inhibition (Fig. 1A) (Fig. S1A). Moreover, trypan blue staining indicated that erastin, sorafenib, and RSL3 treatment markedly resulted in an increase in the dead cells (Fig. S1B). Lipid peroxidation, iron overload, lipid ROS accumulation, and glutathione (GSH) depletion are hallmarks of ferroptotic cells [29]. As expected, treatment with erastin, sorafenib, and RSL3 dramatically increased the end products of lipid peroxidation MDA (Fig. 1B), intracellular redox-active iron overload (Fig. 1C), GSH depletion (Fig. 1D), and lipid ROS accumulation (Fig. S1C). Importantly, ferrostain-1, but not necrostatin-1 and ZVAD-FMK, significantly impaired these classical ferroptotic events in HSC ferroptosis (Fig. 1A–D) (Figs. S1C–E). Overall, these results fully confirmed that erastin, sorafenib, and RSL3 can trigger HSC ferroptosis in vitro.

m^{6}A modification can regulate a variety of cell fates including apoptosis, necroptosis, senescence, and endothelium-mesenchymal transition (EMT). Whether m^{6}A modification is involved in the regulation of HSC ferroptosis? To test this potential possibility, we first examined the levels of m^{6}A modification during HSC ferroptosis. Attractively, m^{6}A RNA methylation quantification assay and dot blot showed a significant increase in m^{6}A modification levels after treatment with sorafenib, erastin, and RSL3 (Fig. 1E and F) (Figs. S1F and 1G). Of note, the protein and mRNA expression of METTL4 rather than other methyltransferase was significantly upregulated (Fig. 1G and H) (Figs. S1H and 1I), whereas the level of FTO rather than other demethylase was markedly downregulated in HSC ferroptosis (Fig. 1I and J) (Figs. S1J and S1K). Collectively, these findings suggested that m^{6}A modification was increased due to the dysregulation of writer METTL4 and eraser FTO during HSC ferroptosis (Fig. 1K).

3.2. Inhibition of m^{6}A modification confers resistance to HSC ferroptosis

HSC-LX2 cells stably transfected with METTL4 shRNA or FTO plasmid were used to investigate whether upregulated m^{6}A modification was directly involved in the induction of ferroptosis (Figs. S2A and 2B). m^{6}A RNA methylation quantification assay confirmed that both METTL4 knockdown and FTO overexpression could completely impair erastin-induced up-regulation of m^{6}A modification in HSC-LX2 (Fig. 2A). Moreover, METTL4 shRNA or FTO plasmid significantly abolished the growth inhibition in HSC-LX2 and HSC-T6 cells by erastin and sorafenib treatment (Fig. 2B). Furthermore, the results showed that m^{6}A modification inhibition by METTL4 shRNA and FTO plasmid evidently damaged erastin- and sorafenib-induced redox-active iron accumulation (Fig. 2C), GSH depletion (Fig. 2D), lipid ROS generation (Fig. 2E), and MDA production (Fig. 2F). Interestingly, in the presence of FTO plasmid, ferroptosis inhibitors including liproxstatin-1 and ferrostain-1 markedly reversed growth inhibition induced by erastin(Fig. 2G), whereas ZVAD-FMK, necrostatin-1, and necrosulfonamide (a potent necroptosis inhibitor that targets mixed lineage kinase domain-like protein), did not effectively reverse this process (Fig. 2G). More importantly, transmission electron microscopy assays confirmed that erastin treatment substantially shanked mitochondria and decreased the number of ridges, whereas FTO plasmid completely abolished the typical changes of ferroptotic cells (Fig. 2H). Overall, these data showed that up-regulation of m^{6}A modification by ferriptosis inducer treatment may contribute to

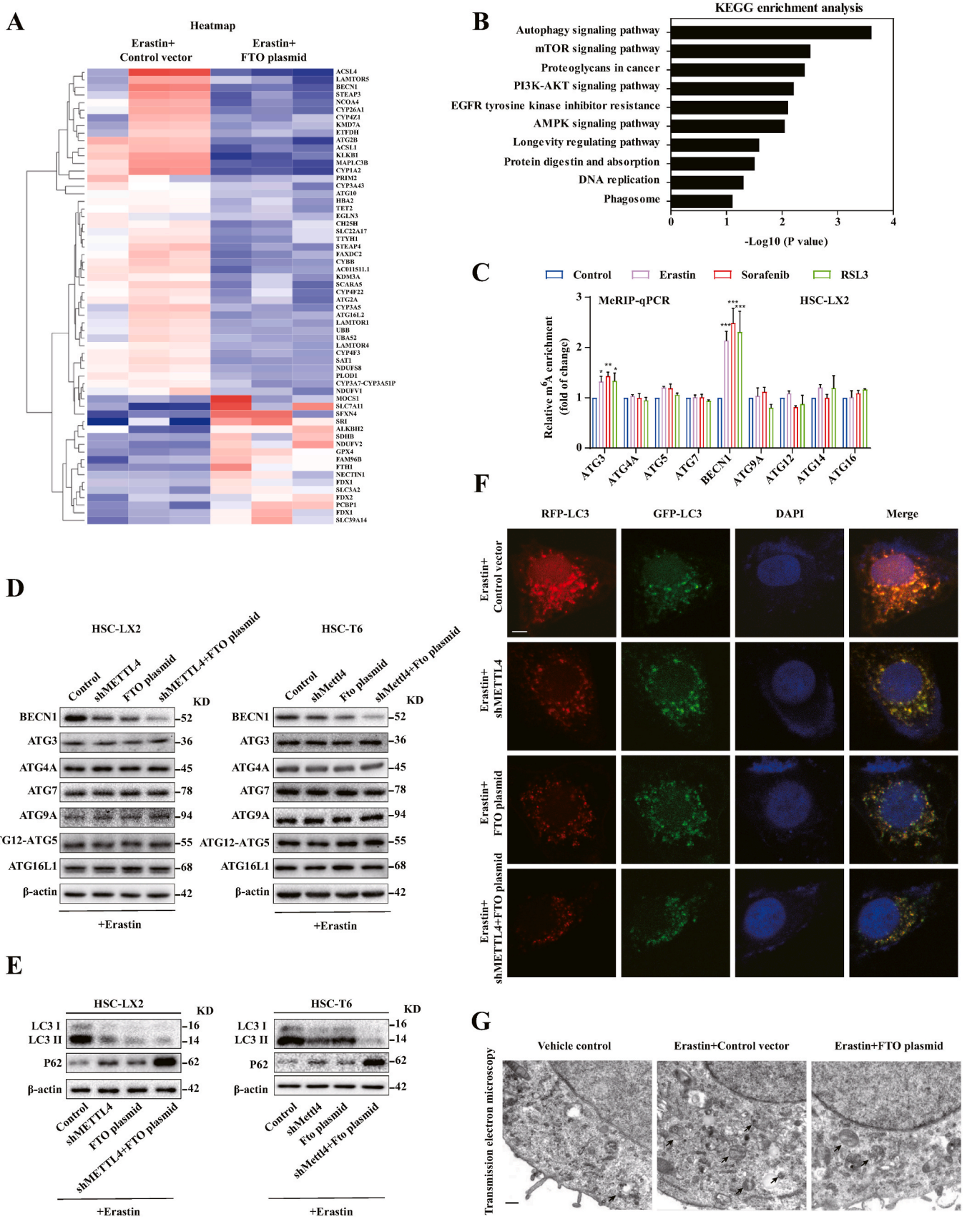

(caption on next page)

Fig. 3. Reduced ferroptosis by m^{6}A modification inhibition is associated with autophagy inactivation. (A) FTO plasmid was transfected into HSC-LX2 cells and treated with erastin (10 μM) for 24 h. Total RNA was isolated for RNA-Seq. Clustering of HSC-LX2 cells were demonstrated by microarray heat map. The significantly differentially expressed mRNAs were analysied by hierarchical cluster: gray, no change; bright blue, underexpression; bright red, overexpression (FTO plasmid, n = 3; Control vector, n = 3). (**B**) Differentially expressed mRNAs were enriched by KEGG enrichment analysis in FTO plasmid group (Control vector, n = 3; FTO plasmid, n = 3). (**C**) The levels of m^{6}A modification in autophagy-related gene were determined by MeRIP qPCR (*, $p < 0.05$, **, $p < 0.01$, ***, $p < 0.001$, n = 3 in every group). (**D**) METTL4 shRNA or FTO plasmid transfected into HSC-T6 and HSC-LX2 cells were treated with erastin (10 μM) for 24 h. Western blot showed the protein expression of BECN1, ATG3, ATG4A, ATG7, ATG9A, ATG5-ATG12 and ATG16L1 (n = 3 in every group). (**E**) Western blot was used to determine the expression of LC3-I/II and p62 (n = 3 in every group). (**F**) METTL4 shRNA or FTO plasmid with CMV-TurboRFP- EGFP-LC3-PGK-Puro plasmid were transferred into HSC-LX2 cells by erastin (10 μM) treatment for 24 h. The fluorescence spots were detected. Representative photographs were showed. Scale bars: 50 μm. (**G**) HSC-LX2 cells transfected with FTO plasmid or control vector by erastin (10 μM) treatment for 24 h. Transmission electron microscopy was used to examine the autolysosomes or autophagosomes. Representative photographs were showed. Scale bars: 0.2 μm. (For interpretation of the references to color in this figure legend, the reader is referred to the Web version of this article.)

HSC ferroptosis, but not necroptosis and apoptosis.

3.3. Reduced ferroptosis by m^{6}A modification inhibition is associated with autophagy inactivation

We further performed RNA sequencing (RNA-seq) to further explore the molecular mechanism by which m^{6}A modification promotes HSC ferroptosis and to identify the target genes involved in the glutamine metabolic pathway, non-classical autophagy pathway and classical iron metabolic pathway. The results showed that 424 mRNAs were significantly increased (fold change >1.4), whereas 317 mRNAs were apparently decreased (fold change <0.65) in FTO overexpressed HSC-LX2

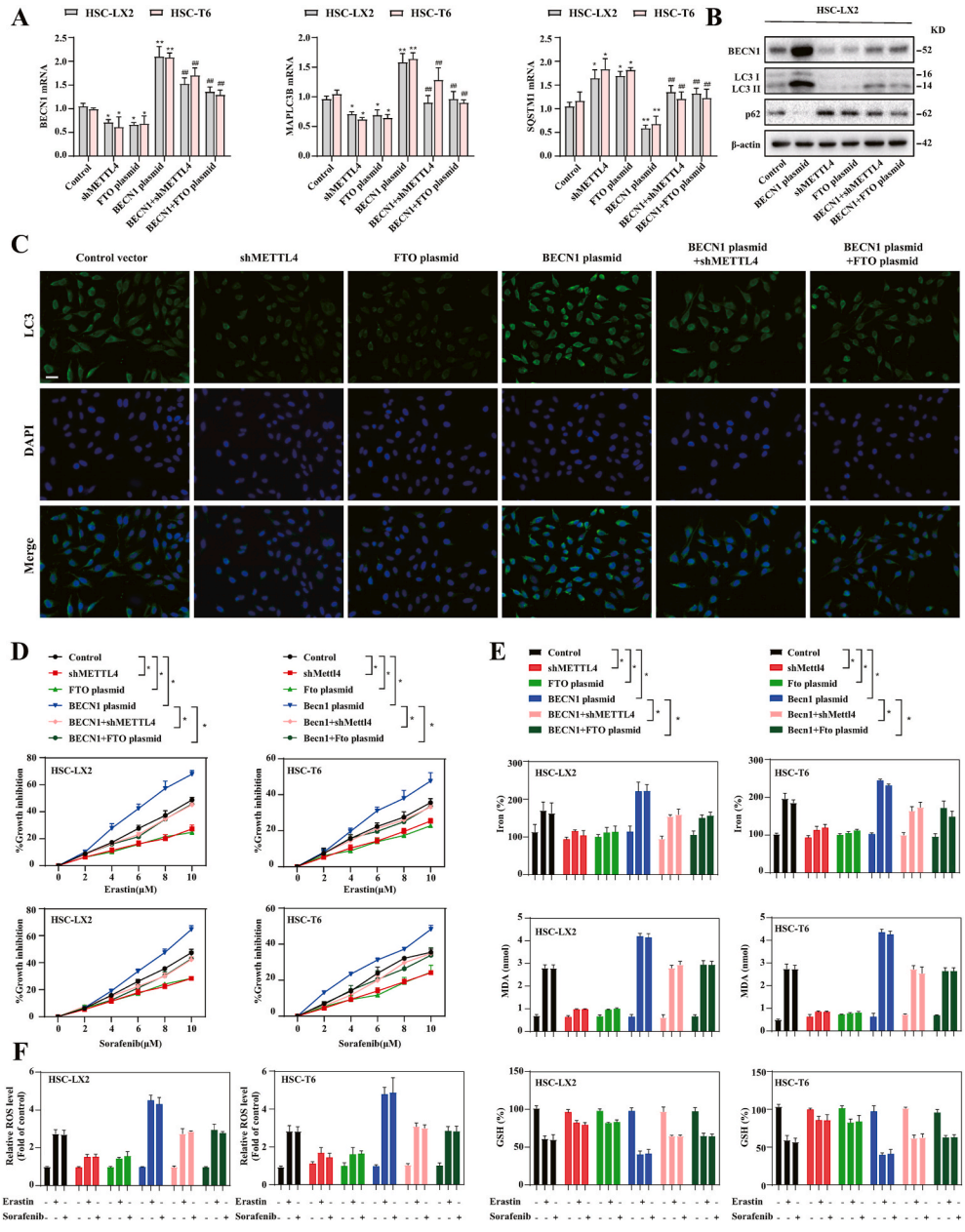

Fig. 4. Induction of autophagy by BECN1 plasmid impairs m^{6}A modification inhibition-induced resistance to HSC ferroptosis. (**A**) BECN plasmid and METTL4 shRNA or FTO plasmid were transfected into HSC-T6 and HSC-LX2 cells and trested with erastin (10 μM) for 24 h. Real-time PCR were used to measure the mRNA levels of BECN1, MAPILC3B and SQSTM1 (*, $p < 0.05$, **, $p < 0.01$, compared with Control group, ##, $p < 0.01$, compared with BECN1 plasmid group, n = 3 in every group). (**B**) Western blot showed the protein expression of p62 and LC3-I/II (n = 3 in every group). (**C**) The endogenous LC3 levels were measured by immunofluorescence (n = 3 in every group). (**D**) HSC-LX2 and HSC-T6 cells transfected with BECN plasmid and METTL4 shRNA or FTO plasmid were treated with erastin (10 μM) or sorafenib (10 μM) for 24 h. Cell viability was assayed by Cell Counting Kit-8 (n = 3 in every group, *, $p < 0.05$). (**E, F**) MDA production, Iron accumulation, GSH depletion and lipid ROS level were assayed by commercial kits (*, $p < 0.05$, n = 3 in every group).

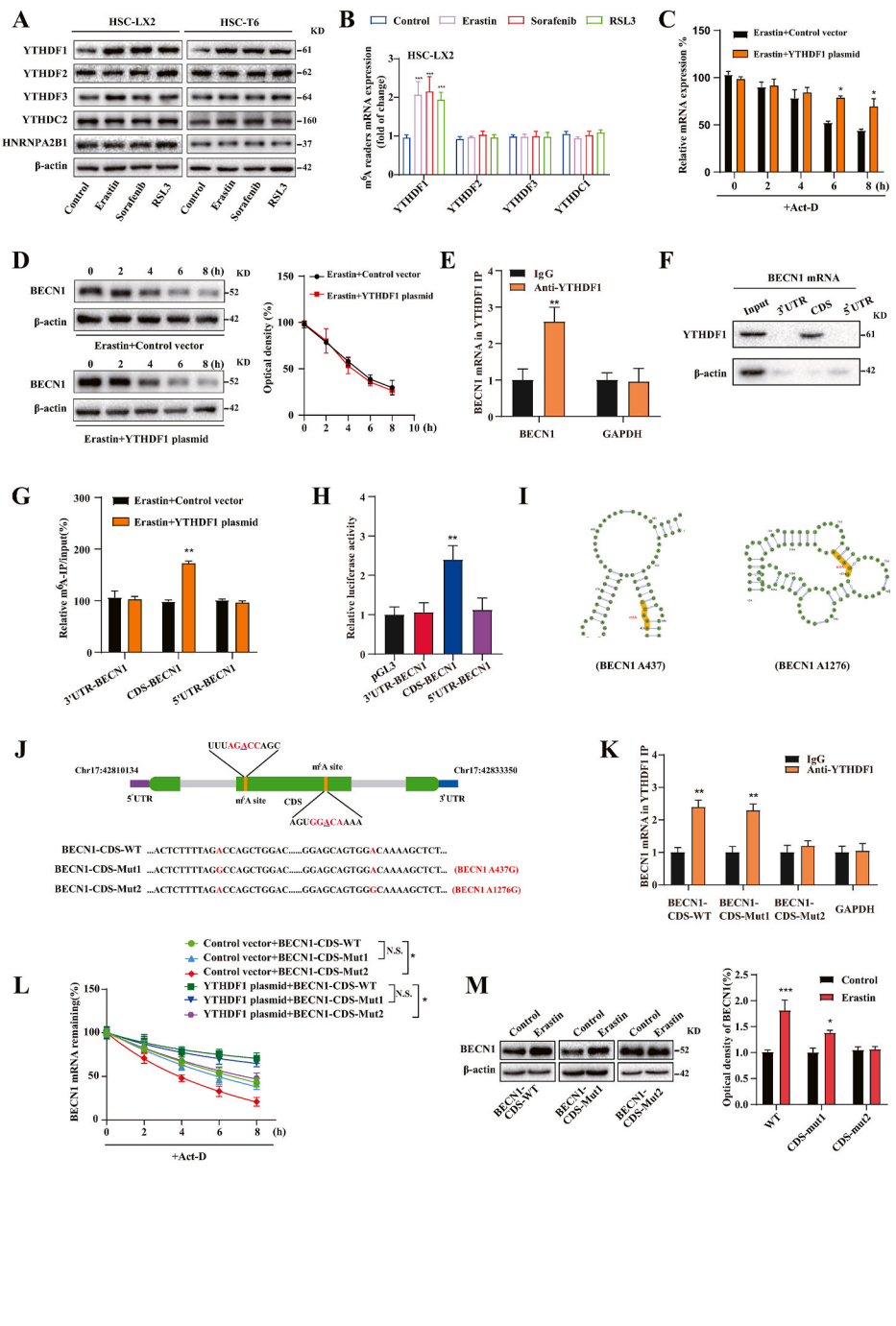

Fig. 5. m^{6}A reader protein YTHDF1 promotes autophagy activation and BECN1 mRNA stability via recognizing the m^{6}A binding site. HSC-T6 and HSC-LX2 cells were added sorafenib (10 μM), erastin (10 μM), and RSL3 (2.5 μM) and treated for 24 h. (**A**) Western blot was used to assay the protein levels of m^{6}A readers (n = 3 in every group). (**B**) The mRNA levels of m^{6}A readers were determined by real-time PCR (***, $p < 0.001$, n = 3 in every group). (**C**) YTHDF1 plasmid or control vector were transfected into HSC-LX2 cells and treated with erastin (10 μM) for 24 h, and then were pretreated with Act-D (5 μg/ml) for indicated times. Real-time PCR was used to measure the remaining BECN1 mRNA levels (*, $p < 0.05$, n = 3 in every group). (**D**) YTHDF1 plasmid or control vector were transfected into HSC-LX2 and treated with erastin (10 μM) for 24 h. Western blot was used to determine the protein levels of BECN1 at different times under the CHX (100 μg/ml) treatment (n = 3 in every group). (**E**) The binding of YTHDF1 and BECN1 mRNA was measured by ribonucleoprotein immunoprecipitation (RNP IP) (**, $p < 0.01$, n = 3 in every group). (**F**) biotinylated transcripts of the BECN1 mRNA 3′-UTR, CDS, 5′-UTR were used for mRNA affinity isolation assay (n = 3 in every group). (**G**) HSC-LX2 cells were transfected with control vector or YTHDF1 plasmid and by erastin (10 μM) treatment for 24 h. The levels of m^{6}A modification in BECN1 mRNA 3′-UTR, CDS and 5′-UTR were determined by MeRIP qPCR (**, $p < 0.01$, n = 3 in every group). (**H**) HSC-LX2 cells were stably transfected with empty vector (pGL3)or luciferase constructs carrying the genes encoding 5′-UTR-BECN1, CDS-BECN1, 3′-UTR-BECN1. Then cells were added erastin (10 μM) and treated for 24 h, and luciferase activities were measured (**, $p < 0.01$, n = 3 in every group). (**I**) BECN1 mRNA m^{6}A binding site was showed. (**J**) Schematic representation of positions of m^{6}A motifs and mutation in CDS within BECN1 mRNA were showed. (**K**) Binding of YTHDF1 with the BECN1-CDS-WT, BECN1-CDS-Mut1 (A437G) and BECN1-CDS-Mut2 (A1276G) in HSC-LX2 were analyzed by YTHDF1 RNP IP (**, $p < 0.01$, n = 3 in every group). (**L**) HSC-LX2 cells were transfected with control vector or YTHDF1 plasmid and BECN1-CDS-WT, BECN1-CDS-Mut1 and BECN1-CDS-Mut2 plasmid, and then were pretreated with Act-D (5 μg/ml) for indicated times. Real-time PCR was used to measure the remaining BECN1 mRNA (*, $p < 0.05$, n = 3 in every group). (**M**) After transfected with BECN1-CDS-WT, BECN1-CDS-Mut1 and BECN1-CDS-Mut2 plasmid, HSC-LX2 cells were treated with erastin (10 μM) for 48 h. The protein expression of BECN1 was measured by western blot (*, $p < 0.05$, ***, $p < 0.001$, n = 3 in every group).

cells as shown in the heat map (Fig. 3A). As expected, some ferroptosis-related genes, such as SLC7A11 (2.63 fold), SLC3A2 (1.75 fold), GPX4 (1.64 fold), were identified among these genes (Fig. S2C). These positive outcomes validated our screen approach. Importantly, Kyoto Encyclopedia of Genes and Genomes (KEGG) analysis and GO analysis fully indicated that autophagy signaling was potentially regulated by m^{6}A modification during HSC ferroptosis (Fig. 3B) (Fig. S2D). Remarkably, we found that the expression of BECN1, a crucial target gene in autophagy signaling, decreased significantly upon FTO overexpression (Fig. S2E). Moreover, m^{6}A RNA-immunoprecipitation (MeRIP) qPCR revealed that the levels of m^{6}A modification in BECN1, but not in ATG3, ATG4A, ATG5, ATG7, ATG9A, ATG12 and ATG16L1, were increased in HSC ferroptosis (Fig. 3C) (Fig. S2F). Consistently, the reduction of m^{6}A modification by FTO plasmid or METTL4 shRNA markedly reduced the protein expression of BECN1 without large differences in other autophagy-related genes (Fig. 3D). It is generally accepted that LC3-II conversion and autophagosome formation require the activation of the conserved BECN1 complex. As expected, the expression of BECN1 and the conversion of LC3-II were increased by erastin treatment (Fig. S2G). While the conversion of LC3-I to LC3-II in erastin induced HSCs was eliminated following reduced m^{6}A modification (Fig. 3E). Meanwhile, immunofluorescence staining and GFP-LC3 puncta formation assay suggested that the down-regulation of m^{6}A modification significantly reduced the expression of endogenous and exogenous LC3 in HSC-LX2 cells (Figs. S2H and S1I). Indeed, HSC-LX2 cells were transfected with CMV-TurboRFP-EGFP- LC3-PGK-Puro plasmid to detect autophagy flux, and the results showed that FTO plasmid and METTL4 shRNA substantially blocked autophagy flux during HSC ferroptosis (Fig. 3F). Besides,

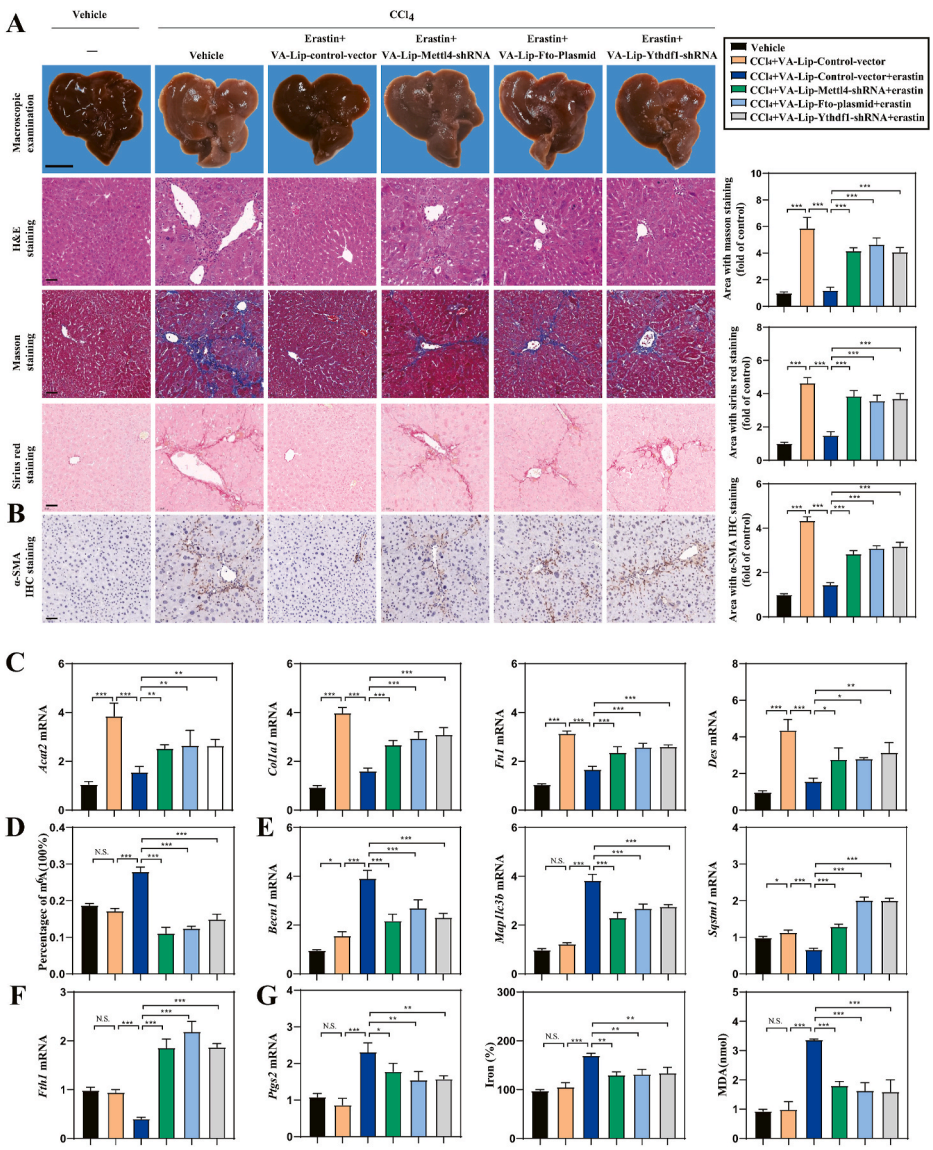

Fig. 6. HSC-specific inhibition of m^{6}A modification impairs erastin-induced HSC ferroptosis in murine liver fibrosis. Mice of 6 groups were treated with Vehicle, CCl_4, CCl_4+VA-Lip-control-vector + Erastin, CCl_4+VA-Lip-Mettl4-shRNA + Erastin, CCl_4+VA-Lip-Fto-Plasmid + Erastin, CCl_4+VA-Lip-Ythdf1-shRNA + Erastin. (**A**) Macroscopic examination was used to observe the pathological changes of the livers. Scale bars: 1 cm. Histopathological study was performed by H&E, Masson, and Sirius Red staining. Representative photographs were showed. Scale bars: 50 μm. (***, $p < 0.001$, $n = 6$ in every group). (**B**) Immunohistochemical staining of α-SMA was determined. Representative photographs were showed. Scale bars: 50 μm.(***, $p < 0.001$, $n = 6$ in every group). (**C**) Real-time PCR was measured to determine the mRNA expression of liver fibrosis markers (Acta2, Col1a1, Fn1, and Des) (*, $p < 0.05$, **, $p < 0.01$, ***, $p < 0.001$, $n = 6$ in every group). (**D**) The m^{6}A levels were determined by m^{6}A RNA Methylation Quantitative kit ($n = 6$ in every group, ***, $p < 0.001$, N.S., not significant). (**E, F**) Real-time PCR was used to determine the mRNA expression of autophagy markers (Becn1, Map1lc3b, Sqstm1, and Fth1) (*, $p < 0.05$, ***, $p < 0.001$, N.S., not significant, $n = 6$ in every group). (**G**) The mRNA expression of Ptgs2, iron accumulation and MDA production were determined (*, $p < 0.05$, **, $p < 0.01$, ***, $p < 0.001$, N.S., not significant, $n = 6$ in every group). (For interpretation of the references to color in this figure legend, the reader is referred to the Web version of this article.)

transmission electron microscopy assays further confirmed that the down-regulation of m^{6}A modification by FTO plasmid reduced autophagic vesicles in HSC ferroptosis (Fig. 3G). Interestingly, the reduction of m^{6}A modification significantly inhibited the autophagic degradation of long-lived protein in the long-lived protein degradation assay (Fig. S2J). Notably, NCOA4-dependent FTH1 degradation plays a central role in facilitating ferritinophagy [30]. As expected, FTO plasmid and METTL4 shRNA markedly impaired erastin-induced upregulation of NCOA4 and downregulation of FTH1 in HSC-LX2 cells (Fig. S2K). Altogether, these data suggested that the induction of ferroptosis by m^{6}A modification was associated with autophagy activation.

3.4. Induction of autophagy by BECN1 plasmid impairs m^{6}A modification inhibition-induced resistance to HSC ferroptosis

We further to estimate whether autophagy inactivation mediated m^{6}A modification inhibition-induced ferroptosis resistance, BECN1 plasmid was employed to activate autophagy. As expected, the results confirmed that BECN1 plasmid completely impaired m^{6}A modification inhibition-induced BECN1 downregulation during HSC ferroptosis (Fig. 4A and B). Moreover, BECN1 overexpression restored the generation of autophagosome (Fig. 4A–C), and autophagic flux (Fig. 4A–C) in the presence of m^{6}A modification reduction. Indeed, erastin and sorafenib-induced growth inhibition was damaged by FTO plasmid and METTL4 shRNA, whereas the BECN1 plasmid dramatically promoted growth inhibition during HSC ferroptosis (Fig. 4D). Similarly, pretreatment with METTL4 shRNA or FTO plasmid completely abolished iron accumulation (Fig. 4E), MDA production (Fig. 4E), GSH depletion (Fig. 4E) and lipid ROS accumulation (Fig. 4F) in HSCs by erastin- and sorafenib treatment. However, m^{6}A modification inhibition did not markedly impair the ferroptotic events in the presence of BECN1 plasmid (Fig. 4E and F). Taken together, these findings showed that activation of autophagy by BECN1 plasmid impaired the resistance of m^{6}A modification inhibition to HSC ferroptosis.

3.5. m^{6}A reader protein YTHDF1 promotes autophagy activation and BECN1 mRNA stability via recognizing the m^{6}A binding site

It has been reported that m^{6}A modification functions in condition of its recognition by m^{6}A reader proteins [31]. Which m^{6}A reader protein mediates the regulation of autophagy-dependent ferroptosis by m^{6}A modification? To address this problem, we performed an unbiased screen among m^{6}A reader proteins. Interestingly, the results showed that YTHDF1 protein and mRNA rather than other m^{6}A readers were

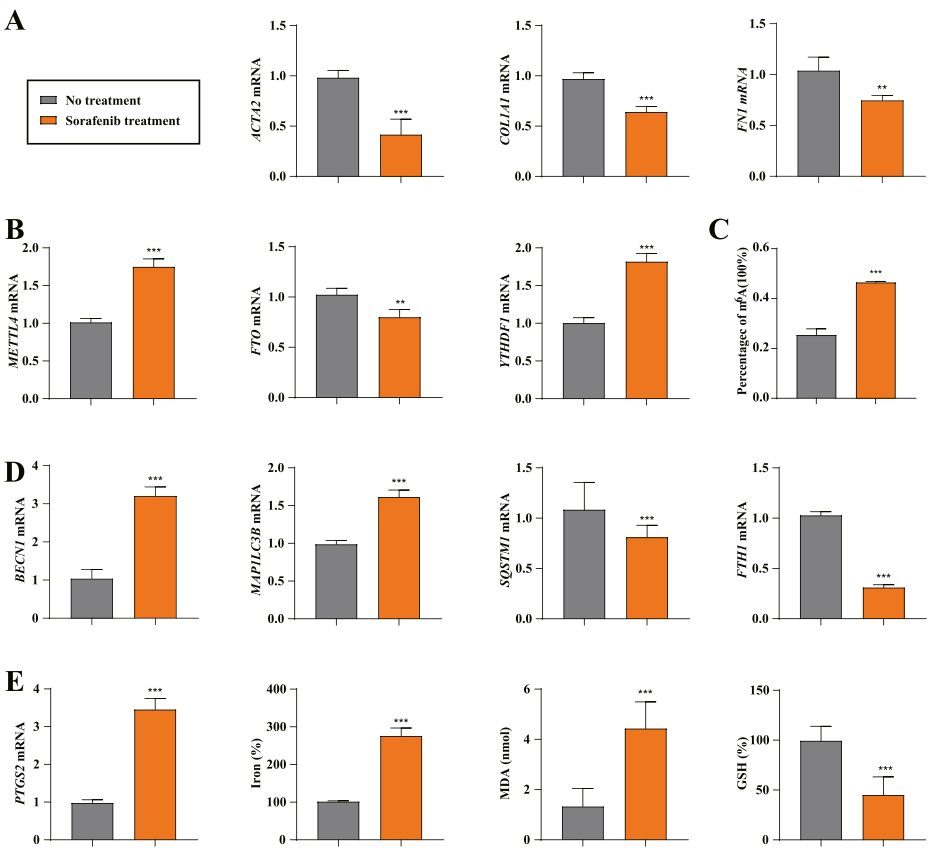

Fig. 7. m^{6}A modification upregulation, autophagy activation, and ferroptosis induction occur in human HSCs receiving sorafenib monotherapy. (**A, B**) laser capture microdissection (LCM) was used to isolated the primary human HSCs from the collected liver tissue. ACTA2, FN1, COL1A1, METTL4, FTO, and YTHDF1 mRNA expression were determined by real-time PCR (No treatment, n = 10; Sorafenib treatment, n = 10, **, p < 0.01, ***, p < 0.001). (**C**) The m^{6}A levels were determined by m^{6}A RNA Methylation Quantitative kit (No treatment, n = 10; Sorafenib treatment, n = 10, ***, p < 0.001). (**D**) Real-time PCR was used to determine the mRNA expression of autophagy markers BECN1, MAP1LC3B, SQSTM1, and FTH1 (No treatment, n = 10; Sorafenib treatment, n = 10, ***, p < 0.001). (**E**) The PTGS2 mRNA expression, iron accumulation, MDA production and GSH depletion were determined (No treatment, n = 10; Sorafenib treatment, n = 10, ***, p < 0.001).

significantly upregulated during HSC ferroptosis (Fig. 5A and B and S3A). Moreover, the results showed that pretreatmet with YTHDF1 shRNA dramatically impaired the induction of BECN1 plasmid on HSC ferroptosis (Fig. S3B). YTHDF1 can recognize m^{6}A methylated mRNA and promotes the post-transcriptional regulation of its targets [32]. Indeed, western blot showed that YTHDF1 shRNA attenuated erastin-induced expression of BECN1 (Fig. S3C). Growing evidence suggest that YTHDF1 binds to the m^{6}A sites of short-lived human transcripts, promoting mRNA stability and translation. We observed that the mRNA half-life of BECN1 in HSC-LX2 cells transfected with YTHDF1 plasmid was prolonged compared with control vector group (Fig. 5C). Consistently, HSC-LX2 cells treated with translation inhibitor cycloheximide showed no significant difference in the protein half-life of BECN1 between YTHDF1 plasmid and control vector group (Fig. 5D). In order to verify whether YTHDF1 bound to the BECN1 mRNA in HSC LX2 cells, the interaction between YTHDF1 and BECN1 mRNA was detected by RNP IP. As shown in Fig. 5E, compared with GAPDH PCR product the BECN1 PCR products were highly enriched in YTHDF1 samples, demonstrating a direct bind of YTHDF1 to BECN1 mRNA. Furthermore, the results of mRNA-protein precipitation showed that YTHDF1 could readily interact with the BECN1 CDS rather than 3′-UTR and 5′-UTR transcripts of BECN1 (Fig. 5F). MeRIP qPCR also showed that m^{6}A modification was significantly enriched in BECN1 CDS (Fig. 5G). Importantly, the luciferase activity was significantly increased in HSC-LX2 cells transfected with the BECN1 CDS (Fig. 5H). Attractively, detailed primary sequence analysis revealed two 5-nucleotide consensus sequence (AGACC, GGACA) in CDS of the BECN1 mRNA sequence (Fig. 5I). To confirm the roles of m^{6}A binding sites on the BECN1 CDS region, BECN1-CDS-WT, BECN1-CDS-Mut1 (A437G) and BECN1-CDS-Mut2 (A1276G) were generated as shown in Fig. 5J. RNP IP assays showed that BECN1-CDS-Mut2, but not BECN1-CDS-WT and BECN1-CDS-Mut1, completely impaired the binding of YTHDF1 and BECN1 mRNA (Fig. 5K). Consistently, the RNA stability assay revealed that YTHDF1 plasmid prolonged the half-life of BECN1-CDS-WT mRNA and BECN1-CDS-Mut1 mRNA, but not BECN1-CDS-Mut2 mRNA (Fig. 5L). Besides, western blot results also indicated that BECN1-CDS-Mut2 evidently damaged erastin-induced upregulation of BECN1 protein (Fig. 5M). Collectively, these data indicated that YTHDF1 plasmid promoted BECN1 mRNA stability via binding to the m^{6}A binding site CDS regions at A1276.

3.6. *HSC-specific inhibition of m^{6}A modification impairs erastin-induced HSC ferroptosis in murine liver fibrosis*

To evaluate whether the inhibition of m^{6}A modification impaired ferroptosis in vivo, vitamin A-coupled liposomes carrying Mettl4 shRNA (VA-Lip-Mettl4-shRNA), Fto plasmid (VA-Lip-Fto-plasmid) and Ythdf1 shRNA (VA-Lip-Ythdf1-shRNA) were generated to inhibit HSC-specific m^{6}A modification in CCl_4-induced mouse model of liver fibrosis (Fig. S4A). Macroscopic examination showed that fibrotic pathological was changed in the model group of liver fibrosis compared with the control group, whereas ferroptosis inducer erastin treatment alleviated CCl_4-induced liver fibrosis (Fig. 6A). Interestingly, pretreatment with VA-Lip-Mettl4-shRNA, VA-Lip-Fto-plasmid and VA-Lip-Ythdf1-shRNA completely damaged the improvement of erastin on liver fibrosis (Fig. 6A). Moreover, hematoxylin and eosin (H&E) staining, masson staining, and sirius red staining indicated that erastin treatment markedly reduced collagen deposition in the central vein (Fig. 6A). Attractively, VA-Lip-Mettl4-shRNA, VA-Lip-Fto-plasmid and VA-Lip-Ythdf1-shRNA evidently reversed the effect of erastin on liver fibrosis (Fig. 6A). Immunohistochemistry staining revealed that VA-Lip-Mettl4-shRNA, VA-Lip-Fto-plasmid and VA-Lip-Ythdf1-shRNA completely abolished the inhibition of erastin on α-SMA (actin, alpha 2, smooth muscle, aorta) expression (Fig. 6B). Furthermore, the results demonstrated that VA-Lip-Mettl4-shRNA, VA-Lip-Fto-plasmid and VA-Lip-Ythdf1-shRNA completely eliminated the mRNA expression of Acta2,

Col1a1, Fn1, and Des,which were inhibited by erastin (Fig. 6C).

We previously reported that ferroptosis inducer erastin could alleviate liver fibrosis by inducing ferroptosis in HSCs, but not in liver sinusoidal endothelial cells, hepatocytes, and macrophages [12]. Then, primary HSCs, hepatocytes, macrophages, and liver sinusoidal endothelial cells (LSECs) were isolated from the livers of fibrotic mice to further elucidate the role of m^6A modification in erastin-induced ferroptosis in HSC. Importantly, VA-Lip-Mettl4-shRNA, VA-Lip-Fto--plasmid and VA-Lip- Ythdf1-shRNA significantly prevented the upregulation of erastin on m^6A modification (Fig. 6D). Besides, VA-Lip-Mettl4-shRNA, VA-Lip-Fto-plasmid and VA-Lip-Ythdf1-shRNA blocked the activation of ferritinophagy by erastin treatment, characterized by decreased Becn1 and Map1lc3b expression and increased Sqstm1 and Fth1 expression (Fig. 6E and F). More importantly, inhibition of m^6A modification by VA-Lip-Mettl4-shRNA, VA-Lip-Fto-plasmid and VA-Lip-Ythdf1-shRNA completely impaired erastin-induced HSC ferroptosis characterized by Ptgs2 (prostaglandin-endoperoxide synthase 2) expression, redox-active iron reduction and MDA elimination (Fig. 6G) in primary HSCs. Interestingly, erastin failed to increase the expression of the ferroptosis marker PTGS2 in primary hepatocytes, macrophages, and LSECs (Fig. S4B). Moreover, treatment with erastin could not trigger redox-active iron reduction and MDA elimination in primary hepatocytes, macrophages, and LSECs (Figs. S4C and 4D). We also examined whether Erastin administration suppressed fibrosis by reducing hepatic CYP2E1 activity. The results showed that Erastin administration did not reduce CYP2E1 activity (Fig. S4E). In conclusion, these results supported the hypothesis that HSC-specific m^6A modification inhibition in murine liver fibrosis impaired erastin-induced HSC ferroptosis.

3.7. m^6A modification upregulation, autophagy activation, and ferroptosis induction occur in human HSCs receiving sorafenib monotherapy

To evaluate the potential mechanism of m^6A modification clinically, the partial hepatectomy specimens from 10 patients with cirrhotic complicated with HCC treated with sorafenib monotherapy and liver biopsy samples from 10 patients with cirrhotic who did not receive any treatment were analyzed. Then, laser capture microdissection was used to isolated the primary HSCs from the collected liver tissue according to previous reports. Consistent with previous findings, the mRNA levels of fibrosis markers ACTA2, COL1A1 and FN1 were significantly decreased in hepatectomy samples treated with sorafenib compared with untreated liver biopsy samples (Fig. 7A). As expected, real-time PCR analysis showed that the expression of METTL4 and YTHDF1 were upregulated, but the expression of FTO was downregulated in sorafenib monotherapy samples (Fig. 7B). m^6A quantified assay demonstrated a significant increase in m^6A modification levels in primary HSCs treated with sorafenib compared to untreated controls (Fig. 7C). Furthermore, sorafenib treatment may upregulate the levels of ferritinophagy markers BECN1 and MAP1LC3B, and downregulate the levels of the ferritinophagy substrates SQSTM1 and FTH1 in human HSCs (Fig. 7D). Importantly, sorafenib treatment increased the expression of ferroptosis marker PTGS2 in primary HSCs, as well as ferroptotic events including redox-active iron overload, lipid peroxidation and GSH deletion (Fig. 7E). Taken together, these findings suggested that sorafenib monotherapy contributed to the upregulation of m^6A modification, activation of autophagy, and induction of ferroptosis in human HSCs from patients with fibrotic.

4. Discussion

Ferroptosis is a newly discovered form of regulated cell death caused by iron-dependent lipid peroxidation, which is essentially different from other well-characterized types of cell death [33]. Further recognition of ferroptosis in the development of liver fibrosis has brought new perspectives for diagnosis and treatment. Attractively, Li et al. recently reported that artemether-induced ferroptosis alleviates liver fibrosis via IRP2/Iron/ROS axis [34]. Furthermore, Kuo et al. found that chrysophanol attenuates liver fibrosis induced by hepatitis B virus X protein by regulating HSC ferroptosis [35]. Consistent with previous researches, we found that ferroptosis inducers significantly inhibited cell viability and alleviated CCl_4-induced liver fibrosis by inducing HSC ferroptosis. Although ferroptosis brings new perspectives for the treatment and prevention of liver fibrosis, the precise role of ferroptosis in liver fibrosis has not been defined and there are still many drawbacks that need to be noticed. Of note, we previously found that ferroptosis inducers sorafenib and erastin could trigger MDA production, lipid ROS accumulation, and redox-active iron overload in HSCs, but not hepatocytes, macrophages, and liver sinusoidal endothelial cells [13]. In fact, many studies have confirmed that sorafenib treatment may exert anti-fibrotic activity in preclinical and clinical studies. Wang et al. showed that sorafenib can inhibit intrahepatic fibrosis, hydroxyproline accumulation and collagen deposition [36]. The sensitivity of liver cells to ferroptosis inducers was different, and specifically targeting HSC ferroptosis will be the research direction in the future.

m^6A has been identified as the predominant internal modification of mRNAs in eukaryotic uncovering the consensus motif RRACH [37]. The m^6A motifs are typically enriched in the 3′-UTR and CDS, which may play a critical role in regulating precursor mRNA maturation, translation and degradation [37]. A large number of studies have fully confirmed that m^6A modification is closely related with various human diseases, and serves as an important role in regulating cell fate including apoptosis, necroptosis, senescence and EMT [27,38]. Interestingly, Wang et al. demonstrated that m^6A modification promotes adipogenesis through activating autophagy [39]. Moreover, Niu et al. reported that m^6A demethylases FTO is up-regulated in human breast cancer, and silencing FTO can significantly inhibit breast cancer cell proliferation and promote cell apoptosis [40]. However, the function and mechanism of m^6A modification in ferroptosis remain unknown. In the present study, we reported that m^6A modification was increased due to the upregulation of methylase METTL4 and the downregulation of demethylase FTO during HSC ferroptosis. Although more experiments are needed to confirm the exact role of m^6A modification in HSC ferroptosis, our results showed a novel function of m^6A modification in addition to regulating apoptosis, necroptosis, senescence and EMT.

Recent studies indicated that cellular autophagy plays an important role in ferroptosis [41,42]. In particular, the activation of selective autophagy such as NCOA4-mediated ferritinophagy, RAB7A-facilitated lipophagy [43], ARNTL-induced clockophagy [44], and PINK1-activated mitophagy [45], has been reported to promote ferroptosis. In the current study, we found that m^6A modification triggered autophagy activation by stabilizing BECN1 mRNA. BECN1 plasmid could impair the inhibitory action of m^6A modification inhibition on HSC ferroptosis. With a better understanding of autophagy-dependent ferroptosis, autophagy may have potential as a target for antifibrotic therapy.

m^6A-binding proteins with YTH domain, including YTHDF1/2/3, YTHDC1/2, have been recognized to be the “readers” of m^6A motif, which can regulate gene expression through recognize and bind to the m^6A modified transcript [46]. Accumulating evidence has demonstrated that YTHDF1 can recognize m^6A methylated mRNA and promote the post-transcriptional regulation of its targets [32]. In HCC, YTHDF1 contributes to the translation of autophagy-related genes ATG2A and ATG14 by binding to m^6A modified mRNA, thus facilitating autophagy and malignancy of HCC [47]. In non-small cell lung cancer (NSCLC), YTHDF1 deficiency inhibits the proliferation of NSCLC cell and the formation of xenograft tumor by regulating the translational efficiency of CDK2, CDK4, and cyclin D1 [48]. In mouse brain, YTHDF1 facilitates translation of m^6A-methylated neuronal mRNAs in response to neuronal stimulation, and this process contributes to learning and memory [49]. During EMT, YTHDF1 promotes the translation activation of

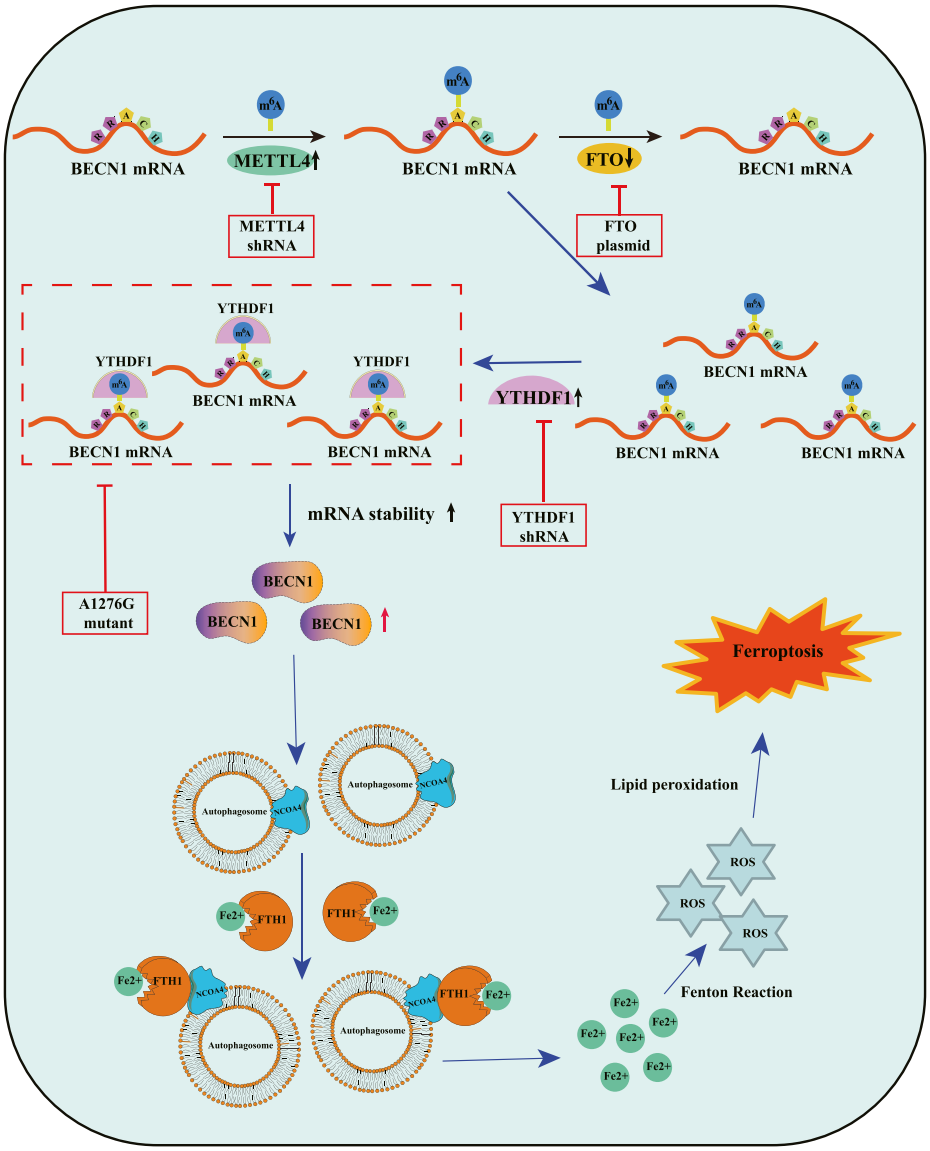

Fig. 8. m^{6}A modification induces HSC ferroptosis by regulating autophagy signaling pathway. The upregulation of methylase METTL4 and the downregulation of demethylase FTO increased the levels of m^{6}A modifications in BECN1 mRNA. m^{6}A reader YTHDF1 promoted BECN1 mRNA stability via recognizing the m^{6}A binding site, thus triggering autophagy activation, and eventually leading to HSC ferroptosis.

m^{6}A-increased Snail mRNA [28]. Importantly, the physiological role of YTHDF1 for the regulation of other tissue needs to be deciphered to distinguish the differential effect of specific m^{6}A modifications during the development of disease. In the present study, we found that YTHDF1 promoted the activation of autophagy and BECN1 mRNA stability via recognizing the m^{6}A binding site within BECN1 CDS at A1276. The mutation of BECN1 m^{6}A sites could abrogate the YTHDF1-mediated BECN1 mRNA stability, and in turn prevented HSC ferroptosis. Our results reveal a new perspective on the potential mechanism by which YTHDF1 regulates ferroptosis.

In summary, we illustrated that the interaction of BECN1 mRNA and m^{6}A modification under ferroptosis inducer treatment enhanced autophagic ferritin degradation, and ultimately causing ferroptosis (Fig. 8). Further analyses of post-transcriptional regulation mechanisms of ferroptosis may provide valuable insights into therapeutic and diagnostic approaches to regulate HSC survival and death in liver fibrosis.

Author contributions

Min Shen did the experiment and analyzed the data. Yujia Li, Yingqian Wang, Jiangjuan Shao, Feng Zhang and Guoping Yin participated in experiments. Anping Chen, Zili Zhang and Shizhong Zheng conceived the idea of study and manuscript writing. All authors had access to the study data and approved the final manuscript.

Declaration of competing interest

The authors declare that they have no known competing financial interests or personal relationships that could have appeared to influence the work reported in this paper.

Acknowledgments

The work was supported by the National Natural Science Foundation of China (82000572, 82073914, 82173874), the Natural Science Foundation of Jiangsu Province (BK20200840), the Major Project of the Natural Science Research of Jiangsu Higher Education Institutions (19KJA310005), General Projects of the Natural Science Research of Jiangsu Higher Education Institutions (20KJB310003), the Joint Project of Jiangsu Key Laboratory for Pharmacology and Safety Evaluation of

Chinese Materia Medica and Yangtze River Pharmaceutical (JKLPSE202005), the Natural Science Foundation of Nanjing University of Chinese Medicine (NZY82000572), the Open Project of Chinese Materia Medica First-Class Discipline of Nanjing University of Chinese Medicine (2020YLKX023, 2020YLKX022) , and Jiangsu Graduate Research and Practice Innovation Program (KYCX21_1738). We are very grateful for the help provided by the experiment center for science and technology of Nanjing University of Chinese Medicine.

Appendix A. Supplementary data

Supplementary data to this article can be found online at https://doi.org/10.1016/j.redox.2021.102151.

References

[1] K. Breitkopf-Heinlein, W.K. Syn, Harnessing liver progenitors in the treatment of liver fibrosis: a step in the right direction? Gut 69 (6) (2020) 975–976.
[2] C.R. Gandhi, Hepatic stellate cell activation and pro-fibrogenic signals, J. Hepatol. 67 (5) (2017) 1104–1105.
[3] S. Wang, S.L. Friedman, Hepatic fibrosis: a convergent response to liver injury that is reversible, J. Hepatol. 73 (1) (2020) 210–211.
[4] M. Bian, J. He, H. Jin, N. Lian, J. Shao, Q. Guo, S. Wang, F. Zhang, S. Zheng, Oroxylin A induces apoptosis of activated hepatic stellate cells through endoplasmic reticulum stress, Apoptosis 24 (11–12) (2019) 905–920.
[5] Z. Zhang, Z. Yao, S. Zhao, J. Shao, A. Chen, F. Zhang, S. Zheng, Interaction between autophagy and senescence is required for dihydroartemisinin to alleviate liver fibrosis, Cell Death Dis. 8 (6) (2017), e2886.
[6] Y. Jia, F. Wang, Q. Guo, M. Li, L. Wang, Z. Zhang, S. Jiang, H. Jin, A. Chen, S. Tan, F. Zhang, J. Shao, S. Zheng, Curcumol induces RIPK1/RIPK3 complex-dependent necroptosis via JNK1/2-ROS signaling in hepatic stellate cells, Redox Biol. 19 (2018) 375–387.
[7] Z. Zhang, S. Zhao, Z. Yao, L. Wang, J. Shao, A. Chen, F. Zhang, S. Zheng, Autophagy regulates turnover of lipid droplets via ROS-dependent Rab25 activation in hepatic stellate cell, Redox Biol. 11 (2017) 322–334.
[8] C. Lu, W. Xu, F. Zhang, J. Shao, S. Zheng, Nrf2 knockdown attenuates the ameliorative effects of ligustrazine on hepatic fibrosis by targeting hepatic stellate cell transdifferentiation, Toxicology 365 (2016) 35–47.
[9] W. Xu, C. Lu, F. Zhang, J. Shao, S. Yao, S. Zheng, Dihydroartemisinin counteracts fibrotic portal hypertension via farnesoid X receptor-dependent inhibition of hepatic stellate cell contraction, FEBS J. 284 (1) (2017) 114–133.
[10] F. Wang, Y. Jia, M. Li, L. Wang, J. Shao, Q. Guo, S. Tan, H. Ding, A. Chen, F. Zhang, S. Zheng, Blockade of glycolysis-dependent contraction by oroxylin a via inhibition of lactate dehydrogenase-a in hepatic stellate cells, Cell Commun. Signal. 17 (1) (2019) 11.
[11] F. Zhang, S. Lu, J. He, H. Jin, F. Wang, L. Wu, J. Shao, A. Chen, S. Zheng, Ligand activation of PPARγ by ligustrazine suppresses pericyte functions of hepatic stellate cells via SMRT-Mediated transrepression of HIF-1α, Theranostics 8 (3) (2018) 610–626.
[12] Z. Zhang, M. Guo, Y. Li, M. Shen, D. Kong, J. Shao, H. Ding, S. Tan, A. Chen, F. Zhang, S. Zheng, RNA-binding protein ZFP36/TTP protects against ferroptosis by regulating autophagy signaling pathway in hepatic stellate cells, Autophagy 16 (8) (2020) 1482–1505.
[13] Z. Zhang, Z. Yao, L. Wang, H. Ding, J. Shao, A. Chen, F. Zhang, S. Zheng, Activation of ferritinophagy is required for the RNA-binding protein ELAVL1/HuR to regulate ferroptosis in hepatic stellate cells, Autophagy 14 (12) (2018) 2083–2103.
[14] Z. Zhang, M. Guo, M. Shen, D. Kong, F. Zhang, J. Shao, S. Tan, S. Wang, A. Chen, P. Cao, S. Zheng, The BRD7-P53-SLC25A28 axis regulates ferroptosis in hepatic stellate cells, Redox Biol. 36 (2020), 101619.
[15] S.J. Dixon, B.R. Stockwell, The role of iron and reactive oxygen species in cell death, Nat. Chem. Biol. 10 (1) (2014) 9–17.
[16] W.S. Yang, R. SriRamaratnam, M.E. Welsch, K. Shimada, R. Skouta, V. S. Viswanathan, J.H. Cheah, P.A. Clemons, A.F. Shamji, C.B. Clish, L.M. Brown, A. W. Girotti, V.W. Cornish, S.L. Schreiber, B.R. Stockwell, Regulation of ferroptotic cancer cell death by GPX4, Cell 156 (1–2) (2014) 317–331.
[17] R. Kang, S. Zhu, H.J. Zeh, D.J. Klionsky, D. Tang, BECN1 is a new driver of ferroptosis, Autophagy 4 (12) (2018) 2173–2175.
[18] W. Hou, Y. Xie, X. Song, X. Sun, M.T. Lotze, H.J. Zeh 3rd, R. Kang, D. Tang, Autophagy promotes ferroptosis by degradation of ferritin, Autophagy 12 (8) (2016) 1425–1428.
[19] X. Deng, R. Su, H. Weng, H. Huang, Z. Li, J. Chen, RNA N6-methyladenosine modification in cancers: current status and perspectives, Cell Res. 28 (5) (2018) 507–517.
[20] L. Muratori, P. Muratori, G. Lanzoni, S. Ferri, M. Lenzi, Application of the 2010 American Association for the study of liver diseases criteria of remission to a cohort of Italian patients with autoimmune hepatitis, Hepatology 52 (5) (2010) 1857–1858.
[21] H. Nagai, T. Kanekawa, K. Kobayashi, T. Mukozu, D. Matsui, T. Matsui, M. Kanayama, N. Wakui, K. Momiyama, M. Shinohara, K. Ishii, Y. Igarashi, Y. Sumino, Changes of cytokines in patients with liver cirrhosis and advanced hepatocellular carcinoma treated by sorafenib, Canc. Chemother. Pharmacol. 73 (2) (2014) 223–229.
[22] K. McDaniel, F. Meng, N. Wu, K. Sato, J. Venter, F. Bernuzzi, P. Invernizzi, T. Zhou, K. Kyritsi, Y. Wan, Q. Huang, P. Onori, H. Francis, E. Gaudio, S. Glaser, G. Alpini, Forkhead box A2 regulates biliary heterogeneity and senescence during cholestatic liver injury in mice, Hepatology 65 (2) (2017) 544–559.
[23] P. Xing, Y. Niu, R. Mu, Z. Wang, D. Xie, H. Li, L. Dong, C. Wang, A pocket-escaping design to prevent the common interference with near-infrared fluorescent probes in vivo, Nat. Commun. 11 (1) (2020) 1573.
[24] X. Liu, J. Liu, W. Xiao, Q. Zeng, H. Bo, Y. Zhu, L. Gong, D. He, X. Xing, R. Li, M. Zhou, W. Xiong, Y. Zhou, J. Zhou, X. Li, F. Guo, C. Xu, X. Chen, X. Wang, F. Wang, Q. Wang, K. Cao, SIRT1 regulates N6-methyladenosine RNA modification in hepatocarcinogenesis by inducing RANBP2-dependent FTO SUMOylation, Hepatology 72 (6) (2020) 2029–2050.
[25] C.A. Opefi, D. Tranter, S.O. Smith, P.J. Reeves, Construction of stable mammalian cell lines for inducible expression of G protein-coupled receptors, Methods Enzymol. 556 (2015) 283–305.
[26] Y. Yang, M. Luo, K. Zhang, J. Zhang, T. Gao, D.O. Connell, F. Yao, C. Mu, B. Cai, Y. Shang, W. Chen, Nedd4 ubiquitylates VDAC2/3 to suppress erastin-induced ferroptosis in melanoma, Nat. Commun. 11 (1) (2020) 433.
[27] T. Song, Y. Yang, H. Wei, X. Xie, J. Lu, Q. Zeng, J. Peng, Y. Zhou, S. Jiang, J. Peng, Zfp217 mediates m^6A mRNA methylation to orchestrate transcriptional and post-transcriptional regulation to promote adipogenic differentiation, Nucleic Acids Res. 47 (12) (2019) 6130–6144.
[28] X. Lin, G. Chai, Y. Wu, J. Li, F. Chen, J. Liu, G. Luo, J. Tauler, J. Du, S. Lin, C. He, H. Wang, RNA m^6A methylation regulates the epithelial mesenchymal transition of cancer cells and translation of Snail, Nat. Commun. 10 (1) (2019) 2065.
[29] X. Sun, Z. Ou, R. Chen, X. Niu, D. Chen, R. Kang, D. Tang, Activation of the p62-Keap1-NRF2 pathway protects against ferroptosis in hepatocellular carcinoma cells, Hepatology 63 (1) (2016) 173–184.
[30] J.D. Mancias, X. Wang, S.P. Gygi, J.W. Harper, A.C. Kimmelman, Quantitative proteomics identifies NCOA4 as the cargo receptor mediating ferritinophagy, Nature 509 (7498) (2014) 105–109.
[31] X. Wang, Z. Lu, A. Gomez, G.C. Hon, Y. Yue, D. Han, Y. Fu, M. Parisien, Q. Dai, G. Jia, B. Ren, T. Pan, C. He, N6-methyladenosine-dependent regulation of messenger RNA stability, Nature 505 (7481) (2014) 117–120.
[32] X. Wang, B.S. Zhao, I.A. Roundtree, Z. Lu, D. Han, H. Ma, X. Weng, K. Chen, H. Shi, C. He, N^6-methyladenosine modulates messenger RNA translation efficiency, Cell 161 (6) (2015) 1388–1399.
[33] D.J. Klionsky, A.K. Abdel-Aziz, S. Abdelfatah, M. Abdellatif, A. Abdoli, S. Abel, et al., Guidelines for the use and interpretation of assays for monitoring autophagy (4th edition)1, Autophagy 17 (1) (2021) 1–382.
[34] Y. Li, C. Jin, M. Shen, Z. Wang, S. Tan, A. Chen, S. Wang, J. Shao, F. Zhang, Z. Zhang, S. Zheng, Iron regulatory protein 2 is required for artemether-mediated anti-hepatic fibrosis through ferroptosis pathway, Free Radic. Biol. Med. 160 (2020) 845–859.
[35] C.Y. Kuo, V. Chiu, P.C. Hsieh, C.Y. Huang, S.J. Huang, I.S. Tzeng, F.M. Tsai, M. L. Chen, C.T. Liu, Y.R. Chen, Chrysophanol attenuates hepatitis B virus X protein-induced hepatic stellate cell fibrosis by regulating endoplasmic reticulum stress and ferroptosis, J. Pharmacol. Sci. 144 (3) (2020) 172–182.
[36] Y. Wang, J. Gao, D. Zhang, J. Zhang, J. Ma, H. Jiang, New insights into the antifibrotic effects of sorafenib on hepatic stellate cells and liver fibrosis, J. Hepatol. 53 (1) (2010) 132–144.
[37] H. Huang, H. Weng, K. Zhou, T. Wu, B.S. Zhao, M. Sun, Z. Chen, X. Deng, G. Xiao, F. Auer, L. Klemm, H. Wu, Z. Zuo, X. Qin, Y. Dong, Y. Zhou, H. Qin, S. Tao, J. Du, J. Liu, Z. Lu, H. Yin, A. Mesquita, C.L. Yuan, Y.C. Hu, W. Sun, R. Su, L. Dong, C. Shen, C. Li, Y. Qing, X. Jiang, X. Wu, M. Sun, J.L. Guan, L. Qu, M. Wei, M. Müschen, G. Huang, C. He, J. Yang, J. Chen, Histone H3 trimethylation at lysine 36 guides m6A RNA modification co-transcriptionally, Nature 567 (7748) (2019) 414–419.
[38] B.S. Zhao, I.A. Roundtree, C. He, Post-transcriptional gene regulation by mRNA modifications, Nat. Rev. Mol. Cell Biol. 18 (1) (2017) 31–42.
[39] X. Wang, R. Wu, Y. Liu, Y. Zhao, Z. Bi, Y. Yao, Q. Liu, H. Shi, F. Wang, Y. Wang, m^6A mRNA methylation controls autophagy and adipogenesis by targeting Atg5 and Atg7, Autophagy 16 (7) (2020) 1221–1235.
[40] Y. Niu, Z. Lin, A. Wan, H. Chen, H. Liang, L. Sun, Y. Wang, X. Li, X.F. Xiong, B. Wei, X. Wu, G. Wan, RNA N6-methyladenosine demethylase FTO promotes breast tumor progression through inhibiting BNIP3, Mol. Canc. 18 (1) (2019) 46.
[41] Z. Wu, Y. Geng, X. Lu, Y. Shi, G. Wu, M. Zhang, B. Shan, H. Pan, J. Yuan, Chaperone-mediated autophagy is involved in the execution of ferroptosis, Proc. Natl. Acad. Sci. U. S. A. 116 (8) (2019) 2996–3005.
[42] M. Gao, P. Monian, Q. Pan, W. Zhang, J. Xiang, X. Jiang, Ferroptosis is an autophagic cell death process, Cell Res. 26 (9) (2016) 1021–1032.
[43] B. Schroeder, R.J. Schulze, S.G. Weller, A.C. Sletten, C.A. Casey, M.A. McNiven, The small GTPase Rab7 as a central regulator of hepatocellular lipophagy, Hepatology 61 (6) (2015) 1896–1907.
[44] M. Yang, P. Chen, J. Liu, S. Zhu, G. Kroemer, D.J. Klionsky, M.T. Lotze, H.J. Zeh, R. Kang, D. Tang, Clockophagy is a novel selective autophagy process favoring ferroptosis, Sci. Adv. 5 (7) (2019), eaaw2238.
[45] C. Li, Y. Zhang, X. Cheng, H. Yuan, S. Zhu, J. Liu, Q. Wen, Y. Xie, J. Liu, G. Kroemer, D.J. Klionsky, M.T. Lotze, H.J. Zeh, R. Kang, D. Tang, PINK1 and PARK2 suppress pancreatic tumorigenesis through control of mitochondrial iron-mediated immunometabolism, Dev. Cell 46 (4) (2018) 441–455.
[46] X. Jiang, B. Liu, Z. Nie, L. Duan, Q. Xiong, Z. Jin, C. Yang, Y. Chen, The role of m6A modification in the biological functions and diseases, Signal Transduct. Target. Ther. 6 (1) (2021) 74.

[47] Q. Li, Y. Ni, L. Zhang, R. Jiang, J. Xu, H. Yang, Y. Hu, J. Qiu, L. Pu, J. Tang, X. Wang, HIF-1α-induced expression of m6A reader YTHDF1 drives hypoxia-induced autophagy and malignancy of hepatocellular carcinoma by promoting ATG2A and ATG14 translation, Signal Transduct. Target. Ther. 6 (1) (2021) 76.
[48] Y. Shi, S. Fan, M. Wu, Z. Zuo, X. Li, L. Jiang, Q. Shen, P. Xu, L. Zeng, Y. Zhou, Y. Huang, Z. Yang, J. Zhou, J. Gao, H. Zhou, S. Xu, H. Ji, P. Shi, D.D. Wu, C. Yang, Y. Chen, YTHDF1 links hypoxia adaptation and non-small cell lung cancer progression, Nat. Commun. 10 (1) (2019) 4892.
[49] H. Shi, X. Zhang, Y.L. Weng, Z. Lu, Y. Liu, Z. Lu, J. Li, P. Hao, Y. Zhang, F. Zhang, Y. Wu, J.Y. Delgado, Y. Su, M.J. Patel, X. Cao, B. Shen, X. Huang, G.L. Ming, X. Zhuang, H. Song, C. He, T. Zhou, m^6A facilitates hippocampus-dependent learning and memory through YTHDF1, Nature 563 (7730) (2018) 249–253.